Index - Final Report

1. Final report

The final report must be prepared in English. Please fill in the following sections of the template.

1.1 Project details

Project title	`Integrated Photovoltaics with Thermoelectrics`
Project identification	Energinet.dk project no. 12045
Name of the programme which has funded the project (ForskVE, ForskNG or ForskEL)	ForskEL
Name and address of the enterprises/institution responsible for the project	Department of Energy Technology, Aalborg University, Pontoppidanstraede 101, Aalborg 9000 Denmark
CVR (central business register)	29 10 23 84
Date for submission	14-11-2014

1.2 Executive summary

The main goal of this small-scale project (budget: 500K DKK) is to investigate the potential of PV cell performance integrated with thermoelectric generators through advanced numerical methods, analytical modeling and by including manufacturing process considerations in the evaluation. The results focus on three main tasks done in this project. In the first task, application of two conventional designs of micro-structured heat sink is studied. In the second task, a comprehensive and coupled hybrid model of photovoltaic cell and thermoelectric generator that can predict the performance of the hybrid model over a wide range of weather variable parameters is proposed. In the third task of the project, a methodology is proposed for fabrication of flexible photovoltaic and thermoelectric modules. The main results of the project are summarized in the following.

Since configuration of the heat sink has a strong influence on the power generation and net power in thermoelectric generators (TEGs), a micro-structured plate-fin heat sink (PFHS) is compared to a modified design of cross-cut heat sink (CCHS) applied to the TEG. The Power generation in the TEG and the required cooling energy in the heat sinks are considered over a range of hot junction temperature and thermal conductivity of the thermoelectric materials. The particular focus of this study is to explore maximum net power in the TEG module. The three-dimensional governing equations for the flow and the heat transfer are solved using the computational fluid dynamics simulation environment in conjunction with thermoelectric characteristics of the TEG over a wide range of inlet flow velocity. The results show that for a particular type of coolant fluid and dimensions of microchannel the maximum net power occurs at lower flow inlet velocity when the hot junction temperature decreases and when the thermal conductivity of the thermoelements is smaller. However, the thermal conductivity of thermoelectric materials does not have strong influence on maximum power generation for the considered heat sink geometries.

A comprehensive model of hybrid photovoltaic and thermoelectric (PVTEG) module is able to predict behaviour of the module for different weather conditions using real weather data input. In the second task of this project, a fully coupled model is developed to predict performance of conventional PV cell and also hybrid PVTEG module over a wide range of weather conditions. This model can predict power generation by the PV cell and TEG and investigate overall efficiency of the PVTEG module through a nonlinear set of equations which consider radiative and convective losses from front and rear surfaces of the modules. A wide range of the variable parameters of weather condition, such as ambient temperature and solar radiation, and also TEG device, such as fill factor and figure of merit of thermoelectric materials are considered in this evaluation. The results illustrate that conversion efficiency of the hybrid PVTEG with conventional thermoelectric materials with ZT=1 is less than conversion efficiency of the PV-only module. However, higher ZT thermoelectric materials can improve the total efficiency compared to the PV-only case. In addition, primary results of hybrid concentrated photovoltaics (CPV) and TEG is able to provide higher efficiency compared to CPV-only. Furthermore, in the last task of the project the pre-studying of the combined flexible Photovoltaic thin film and flexible thermoelectric generator thin film as a sandwich layer for merging on any micro channel heat exchanger or alternatively the solid state heat sink is studied. The description is also based on different aspects as well as the manufacturability of the device for power production which can increase the total electrical output of the sandwich layer device. Further, industrial ability of the production by definition of the proposed material is considered.

1.3   Project results

This section is divided into three sub-sections representing the objectives, methodology used to achieve the expected results, and discussion of the results of the project. Each sub-section reflects consideration of micro-structured heat sink effect on power generation of thermoelectric generator (TEG), modeling of integrated photovoltaic (PV) cells with TEG implemented for real whether conditions and considering of flexible PV and TEG cell as future hybrid technology.

1.3.1   Objectives

TEGs, which convert heat energy to electrical power by means of semiconductor charge carriers due to temperature difference, have been of great interest to the energy research community in recent years. A key factor in TEG systems is co-optimization of the TEG design with its heat sink, where a challenge is to design and develop of effective heat exchanger. The maximum power generation in the TEG can be enhanced with applying effective heat sink. For instance, heat transfer coefficient on the cold junction of the TEG can affect the optimal design of the thermoelements, where the maximum power generation occurs at larger ratio of the thermoelements foot print area as the heat transfer coefficient increases [1]. Using micro-structured heat sinks provides low weight and compact energy system, compared to the conventional types of heat sinks and can increases modularity of the power system. This type of heat sink has been interest of researchers for configuration optimization.

Beside the thermal resistance consideration, the pressure drop is an important factor for optimization of the micro-structured heat sink design, where the performance of the system depends on the required cooling energy [2, 3]. In TEG systems, maximization of net thermoelectric power is more important than enhancement of the power generation. The net power generation is defined as power generation by the TEG minus required pumping power in the heat sink. Higher voltage can be generated in the TEG if the temperature difference of the hot and cold junctions increases by reduction of thermal resistance of the heat sink. One way to reduce the thermal resistance is to enhance the convective heat transfer coefficient by

increase of the mass flow rate in the channels. On the other hand, for a given channel hydraulic diameter, when the mass flow rate increases the required pumping power increases due to rapidly increase of the pressure drop in the channel. High mass flow rate may require higher pumping power than the power generation by the TEG and can cause negative net power in the system [4]. The optimal mass flow rate can be explored at a practical limit on the available required cooling energy by maximizing power generation in the TEG [5].

In this project, the effectiveness of flat-plate heat sinks (FPHSs) and cross-cut heat sink (CCHS) are compared for reduction of the required pumping power and for maximization of the net power generation. A modified design of the fins under the thermoelements is considered, where this design makes a CCHS for the TEG module. The fluid and thermal characteristics in the heat sinks and the TEG are considered over a wide range of mass flow rate in laminar regime by computational methods. Considering the maximum net power in the system, the required cooling energy in the heat sinks is discussed versus the power generation in the TEG for different thermal conductivity of the Bismuth Telluride based thermoelements and imposed hot junction temperatures.

Solar cells combined with thermoelectric devices have been attractive technologies due to the advantage of reliability, silent operation, and absence of moving parts. These have typically been bulky, segregated systems, matched to provide performance enhancement over a narrow operational window. To achieve a high efficiency of solar electrical devices, the main challenge traditionally is low efficiency of power conversion (electric power produced versus solar radiation). However, the performance of the solar cells can be elevated by not only the improvement of the materials but also the progress of system design. During operation, a portion of the solar radiation converted to thermal energy and increases the temperature of the PV cell, causing the efficiency to decrease. This temperature difference with ambient provide can be suitable to apply TEG devices and make a hybrid power generation system. Integration of the TEG with PV cells may enhance converting a fraction of the heat transferred to electricity to supplement that produced by the PV cell.

In order to improve the overall conversion efficiency of the solar radiation, some research [6, 7] and companies [8, 9] have mostly focused on hybrid photovoltaic and thermoelectric generators, while a few of them [10] considers the effect of the heat sink on the device performance. Mizoshiri et al. [11] reported a hybrid micro-power module consisting of a hot mirror that focuses the solar light on the hot side of the thin-film thermoelectric module. They could increase the open circuit voltage of the thermal-photovoltaic hybrid generator by 1.3% compared to that of the photovoltaic module only. Furthermore, using the micro-scale photovoltaic–thermoelectric hybrid device, Wang et al. [12] could achieve overall conversion efficiency larger than 13% for low-energy photons. The major challenge in integration of PV cell and TEG is that by applying the TEG to the PV cell, thermal resistance of the module increases. The higher temperature in the PV cell causes lower electrical conversion efficiency by the PV cell. Therefore, influence of the TEG application on the PV cell needs to be evaluated carefully.

To understand possibility of using the best and suitable material which makes the flexible PVTEG product more energy competitive, we have to look at the material and processes for a sandwich construction made of two layers and bonded to each other. Thin film silicon photovoltaic cells have normally a configuration classification which is referred to their deposition process. This configuration is not limited to choice of a suitable substrate and therefore the industrial manufacturer of the PV can in fact use a transparent or rigid as well as flexible substrate based on poly-ethylene. Because of the easy roll to roll processing of flexible substrate it has remained the main application of the N-I-P cells, which are connected to the flexible substrate. The cells on this substrate made of the crystalline silicon cells, which are connected to one another and form a crystal lattice. This crystal lattice is a solid state material and forms the PV cells semiconductor.

1.3.2 Methods

1.3.2.1 Governing equations for TEGs

The effect of radiation and natural convection heat transfer are neglected in this study, and the surfaces exposed to the surroundings are assumed to be insulated. Under steady-state condition, the electric field is irrational and the well-known coupled equations of thermoelectric constitutive [13] including both the heat flow and the continuity of electric charge equations are [14]:

$$\nabla.([\Pi].J) - \nabla.([k_{\text{teg}}].\nabla T) = \dot{q}, \tag{1}$$

$$\nabla.([\sigma].[\alpha].\nabla T) + \nabla.([\sigma].\nabla \varphi) = 0. \tag{2}$$

The maximum power generation by the TEG occurs at the matched load, where the internal electrical resistance of the uni-couple is equal to the imposed electrical load resistance [15]:

$$P_{\text{teg-max}} = \frac{(\alpha \Delta T)^2}{4R}. \tag{3}$$

The internal resistance of the TEG in (3) is as follows [1]:

$$R = n \times (R_{\text{n}} + R_{\text{p}}) = n \times \left[\left(\sigma_{\text{n}} \frac{A_{\text{n}}}{H_{\text{n}}} \right)^{-1} + \left(\sigma_{\text{p}} \frac{A_{\text{p}}}{H_{\text{p}}} \right)^{-1} \right]. \tag{4}$$

1.3.2.2 Heat transfer and fluid mechanics in heat sink governing equations

To calculate distribution of velocity and temperature for laminar and incompressible flow in the heat sinks the following continuity, momentum and energy equations are solved [16]:

$$\nabla.\vec{V} = 0, \tag{5}$$

$$\rho_{\text{f}}(\vec{V}\nabla.\vec{V}) = -\nabla p + \mu_{\text{f}}\nabla^2\vec{V}, \tag{6}$$

$$\rho_{\text{f}}c_{\text{f}}(\vec{V}.\nabla T) = k_{\text{f}}\nabla^2 T. \tag{7}$$

The rate of heat removal from the heat sink to the coolant flow is:

$$Q = \dot{m}c_{\text{f}}(T_{\text{o}} - T_{\text{i}}). \tag{8}$$

The required pumping power for the flow is related to the pressure drop and the volumetric flow rate in the heat sinks and can be calculated as follows:

$$P_{\text{pump}} = \Delta p W. \tag{8}$$

The pressure drop in the heat sink is an important factor that influences net power of the module. The net power supplied by the TEG is the power generation by the TEG minus the required pumping power.

$$P_{\text{net}} = P_{\text{teg}} - P_{\text{pump}}. \tag{9}$$

Nomenclature section of Appendix A defines the mentioned parameters above.

1.3.2.3 Integrated model for PV and TEG

Efficiency of PV cell has been traditionally represented with linear expression as follows [17]:

$$\eta_{pv} = \eta_{T_{ref}}[1 - \beta_{ref}(T_{pv} - T_{ref})] \tag{10}$$

where $\eta_{T_{ref}}$ is cell's electrical conversion efficiency at the reference temperature ($T_{ref} = 25\,°C$), and reference solar radiation ($G_{ref} = 1000\ W/m^2$) [18]. In (10) β_{ref} is the cells' temperature coefficient that normally given by its manufacturer and not only depends on the PV martial but also on the reference temperature, and is defined as follows [19]:

$$\beta_{ref} = \frac{1}{T_0 - T_{ref}} = \frac{1}{270\,°C - 25\,°C} \approx 0.004 \tag{11}$$

where T_0 is the temperature at which the efficiency of the cell drops to zero, and for crystal-line silicon cells is equal to $270\,°C$ [20].

For a real environment condition radiative heat loss from front surface of the cell (Q_{rad}) and convective heat loss from front glass cover and rear ethylene vinyl acetate (EVA) layer ($Q_{conv,t}$ and $Q_{conv,b}$ respectively) needs to be modeled. EVA layer is used to encapsulate the silicon cells. Figure 1 illustrates the PV model studied in this project. The electrical power generation by the module for a given solar radiation (G_t) can be:

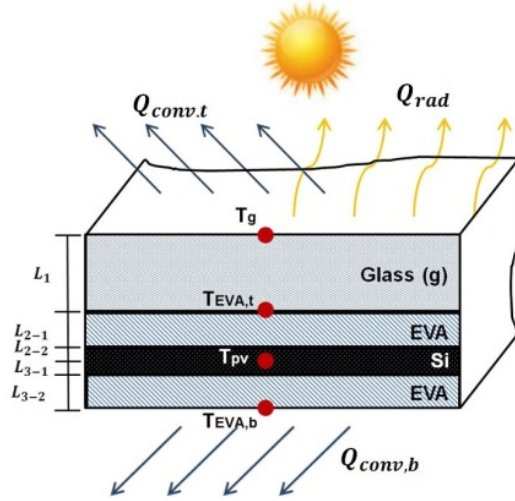$$P_{pv-only} = \eta_{pv}(G_t - Q_{conv,t} - Q_{rad}) \tag{12}$$

Figure 1 PV model studied in this project.

The convective heat loss from surfaces of the glass and EVA layers are:

$$Q_{conv,t} = h_w A_c (T_g - T_a) \tag{13}$$

$$Q_{conv,b} = h_w A_c (T_{EVA,b} - T_a) \tag{14}$$

where A_c is the cell area, T_g is temperature of the glass and $T_{EVA,b}$ is temperature on the rear surface of EVA layer. For a given ambient temperature (T_a) and wind speed (V_m) the convective heat transfer on the surfaces (h_w) is given by Palyvos [21]:

$$h_w = 5.678 \left\{ a + b \left[\left(\frac{294.26}{273.16 + T_a} \right) V_m / 0.3048 \right]^n \right\} \tag{15}$$

In (15) a, b and n are empirical constants given by Table 1 for smooth surfaces texture [22].

Table 1 Values for empirical constants in (15).

$V_m < 4.88\ m/s$			$4.88 < V_m < 30.48\ m/s$		
a	b	n	a	b	n
0.99	0.21	1	0	0.50	0.78

The radiative heat loss from the PV cell depends can be important when the temperature of the cell is relatively high due to high solar radiation and low wind speed:

$$Q_{rad} = \varepsilon \sigma A (T_{pv}^{\ 4} - T_{sky}^{\ 4}) \tag{16}$$

In (16) $\varepsilon = 0.9$ is emissivity of the PV cell equal to 0.9 and $\sigma = 5.67 \times 10^{-8}\ W/m^2 K^4$ is Stefan-Boltzmann constant. By taking energy balance equation for the nodes of PV cell shown in Figure 1, a set of matrix can represent nonlinear equations for four nodal temperatures and

electrical power generation by the PV cell along with the constant vector in matrix a of Table 2.

Table 2 Matrix coefficients for the nonlinear set of four governing equations based on nodal temperatures.

$$\boldsymbol{a} = A_c \begin{bmatrix} H_{wh} + \dfrac{k_g}{L_1} & -\dfrac{k_g}{L_1} & 0 & 0 \\[2mm] -\dfrac{k_g}{L_1} & \dfrac{k_g}{L_1} + \dfrac{k_{EVA}}{L_{21}} + \dfrac{k_{Si}}{L_{22}} & -\dfrac{k_{EVA}}{L_{21}} + \dfrac{k_{Si}}{L_{22}} & 0 \\[2mm] 0 & -\dfrac{k_{EVA}}{L_{21}} - \dfrac{k_{Si}}{L_{22}} & \dfrac{k_{EVA}}{L_{21}} + \dfrac{k_{Si}}{L_{22}} + \dfrac{k_{Si}}{L_{31}} + \dfrac{k_{EVA}}{L_{32}} - \dfrac{G_t \eta_{T_{ref}} \beta_{T_{ref}}}{A_c} & -\dfrac{k_{Si}}{L_{31}} - \dfrac{k_{EVA}}{L_{32}} \\[2mm] 0 & 0 & -\dfrac{k_{Si}}{L_{31}} - \dfrac{k_{EVA}}{L_{32}} & \dfrac{k_{Si}}{L_{31}} + \dfrac{k_{EVA}}{L_{32}} + H_{wc} \end{bmatrix}$$

$$\boldsymbol{b} = \begin{bmatrix} G_t + A_c H_{wh} T_a + \varepsilon \sigma A_c \left(T_{pv}{}^4 - T_{surr}{}^4 \right) \\ 0 \\ G_t \eta_{T_{ref}} \left(1 + \beta_{T_{ref}} T_{ref} \right) \\ A_c H_{wc} T_a \end{bmatrix}$$

The hybrid model of photovoltaic cell and thermoelectric generator (PVTEG) is shown in Figure 2 where seven nodal temperatures represent temperature distribution in the PVTEG model.
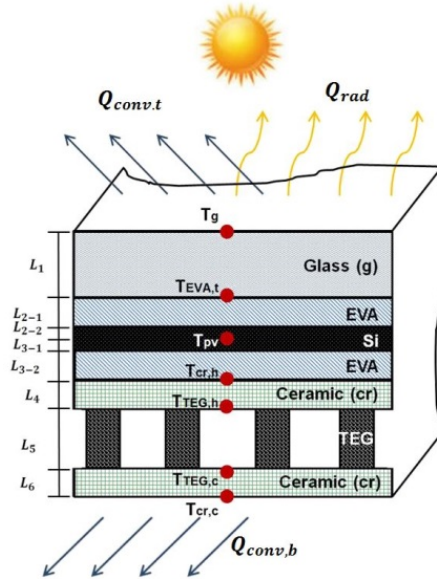

Figure 2 PVTEG model studied in this project.

Based on this temperature distribution, the power generation by the PV cell and the TEG can be obtained. Efficiency of the TEG for constant property model of thermoelectric materials is [23]:

$$\eta_{teg} = \frac{\Delta T_{teg}}{T_{teg,h}} \frac{\sqrt{1 + ZT} - 1}{\sqrt{1 + ZT} + \dfrac{T_{teg,c}}{T_{teg,h}}} \tag{17}$$

Power generation in the TEG depends on efficiency of the TEG and heat transfer across the thermoelements (q_h). Therefore, the power generation by the PV cell and radiative and convective heat losses must be deducted from the solar radiation. The power generation in the TEG is:

$$P_{teg} = \eta_{teg} q_h = \eta_{teg} \left(G_t - Q_{conv,t} - Q_{rad} - P_{pv} \right) \tag{18}$$

To calculate convective and radiative heat losses, (13) - (16) can be applied for PVTEG model, except the cold surface temperature of the EVA surface ($T_{EVA,b}$) is replace with the cold junction temperature of the TEG ($T_{cr,b}$). Therefore by taking the energy balance equations for the PVTEG model, the coupled temperature of the considered nodes can be found by a set of nonlinear equations as follow:

$$\left(A_c H_{wh} + \frac{A_c k_g}{L_1}\right) T_g - \left(\frac{A_c k_g}{L_1}\right) T_{EVA,t} = G_t + A_c H_{wh} T_a + \varepsilon \sigma A_c \left(T_{pv}{}^4 - T_{surr}{}^4\right) \tag{19}$$

$$-\left(\frac{A_c k_g}{L_1}\right) T_g - A_c \left(\frac{A_c k_{pv}}{L_1} + \frac{k_{EVA}}{L_{21}} + \frac{k_{Si}}{L_{22}}\right) T_{EVA,t} + A_c \left(-\frac{k_{EVA}}{L_{21}} + \frac{k_{Si}}{L_{22}} + G_t \eta_{T_{ref}} \beta_{T_{ref}}\right) T_{pv} = 0 \tag{20}$$

$$-A_c \left(\frac{k_{EVA}}{L_{21}} + \frac{k_{Si}}{L_{22}}\right) T_{EVA,t} + A_c \left(\frac{k_{EVA}}{L_{21}} + \frac{k_{Si}}{L_{22}} + \frac{k_{Si}}{L_{31}} + \frac{k_{EVA}}{L_{32}} - \frac{G_t \eta_{T_{ref}} \beta_{T_{ref}}}{A_c}\right) T_{pv} - A_c \left(\frac{k_{Si}}{L_{31}} + \frac{k_{EVA}}{L_{32}}\right) T_{cr,h} =$$
$$-G_t \eta_{T_{ref}} \left(1 + \beta_{T_{ref}} T_{ref}\right) \tag{21}$$

$$-\left(\frac{k_{Si}}{L_{31}} + \frac{k_{EVA}}{L_{32}}\right) T_{pv} + \left(\frac{k_{Si}}{L_{31}} + \frac{k_{EVA}}{L_{32}} + \frac{k_{cr,h}}{L_4}\right) T_{cr,h} - \left(\frac{k_{cr,h}}{L_4}\right) T_{TEG,h} = 0 \tag{22}$$

$$-A_c \left(\frac{k_{cr,h}}{L_4}\right) T_{cr,h} + \left(\frac{A_c k_{cr,h}}{L_4} + \frac{A_{TEG} k_{TEG}}{L_5}\right) T_{TEG,h} - \left(\frac{A_{TEG} k_{TEG}}{L_5}\right) T_{TEG,c}$$
$$= -0.5 \left(\frac{T_{TEG,h} - T_{TEG,c}}{T_{teg,h}}\right) \left(\frac{\sqrt{1+ZT} - 1}{\sqrt{1+ZT} + \frac{T_{TEG,c}}{T_{TEG,h}}}\right) \left(G_t - G_t \eta_{T_{ref}} \left(1 - \left(\beta_{T_{ref}} \left(T_{pv} - T_{ref}\right)\right)\right)\right) \tag{23}$$

$$-\left(\frac{A_{TEG} k_{TEG}}{L_5}\right) T_{TEG,h} + \left(\frac{A_{TEG} k_{TEG}}{L_5} + \frac{A_c k_{cr,c}}{L_6} +\right) T_{TEG,c} - \left(\frac{A_c k_{cr,c}}{L_6}\right) T_{cr,c}$$
$$= -0.5 \left(\frac{T_{TEG,h} - T_{TEG,c}}{T_{teg,h}}\right) \left(\frac{\sqrt{1+ZT} - 1}{\sqrt{1+ZT} + \frac{T_{TEG,c}}{T_{TEG,h}}}\right) \left(G_t - G_t \eta_{T_{ref}} \left(1 - \left(\beta_{T_{ref}} \left(T_{pv} - T_{ref}\right)\right)\right)\right) \tag{24}$$

$$-\left(\frac{A_c k_{cr,c}}{L_6}\right) T_{TEG,c} + A_c \left(\frac{k_{cr,c}}{L_6} + H_{wc}\right) T_{cr,c} = A_c H_{wc} T_a \tag{25}$$

When the one dimension (1D) temperature distribution in the PVTEG model is reached, the electrical power generation by the PV cell and the TEG is calculated. The total efficiency of the PVEG is defined as total electrical power generation for solar radiation on the PVTEG module:

$$\eta_{total} = \frac{P_{pv} + P_{teg}}{G_t} \tag{26}$$

1.3.2.4   Flexible PV-TEG technology

As mentioned the bonding process of the ready PV layer to the manufactured thermoelectric (TE) layer is one of the important cases regarding the sandwich flexibility and heat transfer through the flexible PV film (Figure 3) to the TE-film.

TEG-substrate: The second layer "TE-layer" can be made of commercially semiconductor material as well as bismuth telluride to obtain the power generation from the heat flux through the first layer perpendicular to the second layer. These materials have almost the same strength and mechanical property as the PV material, but they are made by two different manufacturing processes. Different material for the TE substrate has to be studied for selection of the right approach for manufacturability and quality, and to the monotonous

interaction of the layers. The selection of the layer for texturing and implementation of the TE material is divided into two categories.
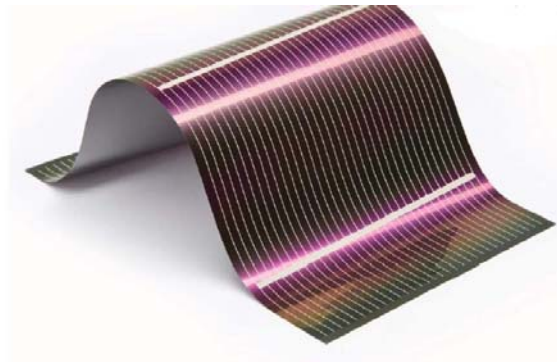

Figure 3 Flexible PV [http://www.cleantechinvestor.com].

The first category is the material of the layer and the second category is the preparation for printing process.

Selected Material for TE- substrate/layer: as shown in Figure 4, the PVTE layer contains of 5 different micro layers which are bonded together and they can make a final 550 micron tick multilayer. The layer starts from the hot side and is explored and explained as below:
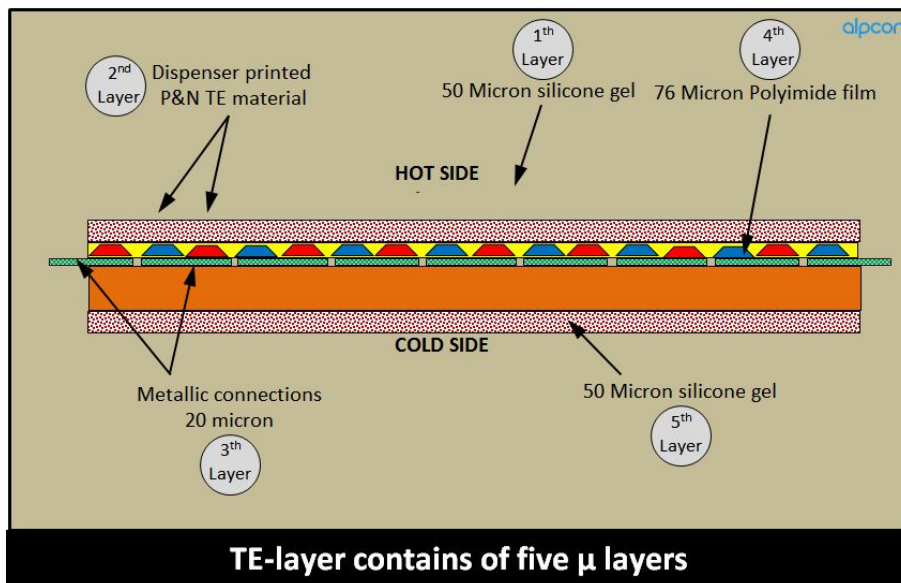

Figure 4 PVTE layer with five micro layers

1.3.2.4.1   1th Micro layer of PVTE

This layer is the bonding layer low toxic, thermal conductive silicon substance. The layer of the PV and eventually the layer of the micro channels for active cooling will be connected together by using preferably a micro layer of bonding that the process based on chemical bonds. This substance will be used by coating process at room temperature.

The coating will be applied to the surfaces between PV substrate/layer and the TE-substrate/layer, furthermore between the TE-layer and the micro channels surface. The direct bonding process gives very good property concerning the radios of the flexibility and the

sandwich layer performance in process of time. This will improve the longer operative life time when the sandwich layers are thermally stressed. This means the layers exposed to sever temperature fluctuations during the sun radiation on the surface of photovoltaic layer (increased temperature) and during the dark period and winter time (decreased temperature). Not suitable bonding can affect to the poor heat transfer through the silicon film to the thermoelectric layer.

By wafer bonding technique is possible to process almost all kind of the material if the surfaces fulfil the requirement, but as silicon is more popular in chemical industry it is most established material for bonding process called direct bonding or by coating process. For the processing this layer over the TE-material the coating method will be applied to the both outer surfaces and will be protected by a preliminary paraffin paper before sandwich assembly of the layers. This coating layer has a thickness of around 50 micron. The accuracy of the thickness depends on which kind of industrial methods will be chosen for this process. However small variation of the thickness have influence on the heat flux of the assembled device.

1.3.2.4.2   2nd Micro layer of PVTE (thermoelectric material)

Substrate printing method and dispenser printed thermoelectric material is a relatively new but is promising and unique method to producing a thick or thin film thermoelectric material with good thermoelectric property especially for operation temperature below 120 ^{o}C. All of the processes for dispenser printing happen on the 4th micro layer with a layer thickness of 100-200 micron depend on the design and flexibility radius. The layer No. 4 is the substrate for TE material and will be manufactured by using one of the most industrially valuable polyimides which is polypyromellitimides and hereafter prepared for dispenser printing. Alternatively the main layer (Layer No. 4) can also be supplied by one of the supplier of the polyimide.

For printing process and producing a good composite, the particle size for the ink must be measured and a micro size particle suitable for this process has to be achieved, therefore the process of quench, ball milling and laser scattering particle size of thermoelectric powder material must be done very carefully. Before making the micro powder the process starts by removal of TE ingot surface impurities such as dust/oxidations/fat and other impurities. Very often the surface of ingot will be contaminated in process of time. After cleaning the ingot it has to be crashed in pieces of max. 6 mm. The grinding process starts by moving the Jar from Argon chamber and place it in the ball mill machine. The duration time for ball milling must not leads to raising the temperature of the Jar and material beyond 50°C.

The result of this process will be a suitable micro Grain size of Powder. The Laser scattering particle size distribution must also be used to shows a roughly compatible size of grains for using in printing process.

Alternative for dispenser printing is; using the newest technology which is under test at Fraunhofer, Institute for Material and Beam Technology IWS, Germany. As the AAU is already involved in FP7 project and have cooperation with Fraunhofer, then it will be an obvious topic for more cooperation with this partner on 3D printing of TEG on thin film. The 3D printing technology at Fraunhofer is one of the achievements of Dr. Aljoscha Roch and his colleagues at IWS. Using this method will result to a quicker success for AAU´s innovative technology. This process is based on using a non-toxic TE-active polymer, which is flexible and will be printed in μm layer on the surface of a Polyimide film (Figure 5).
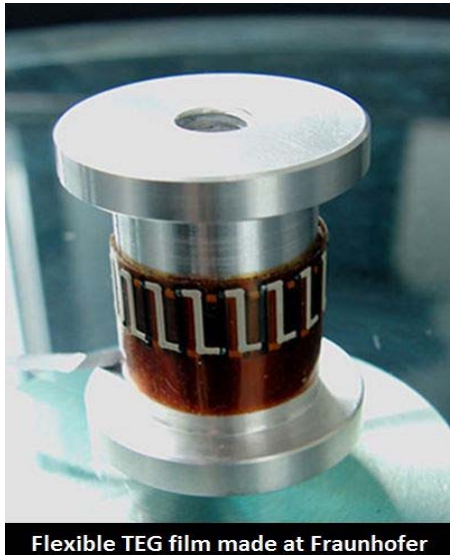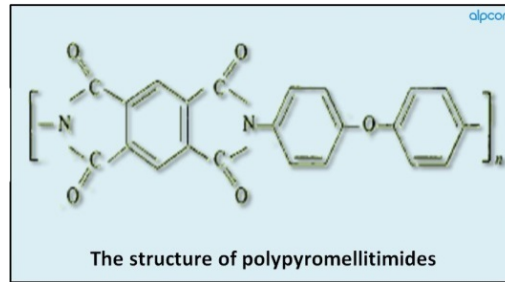
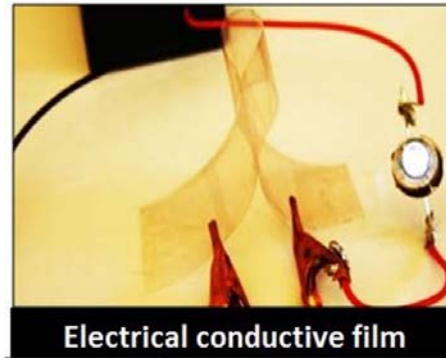*Figure 5 3D printing process of TEG on thin film.*

1.3.2.4.3   3rd Micro layer of PVTE (metallic contact)

This micro layer is a metallic coated or printed layer of either silver Nano wires or carbon nanoparticles. The micro layers making the bridge connections between P&N bonds and P&N dots. This process can be done with any metallic Nano powder with low electrical resistivity. Very good electrical conductivity can be obtained by using the silver Nano wires or silver pasta for metallic connection. A silver Nano wire film (Figure 6) can be transparent and with a size of 40-50 µm can be synthesized in present of Pt seeds and dispersed in a water-based solvent. The thickness of the printed such silver additive ink is decisive factor for the electrical conductivity of the metallic layer. These electrical conductive bridges can be printed by inkjet printing on the flexible polyimide film substrate which is described above (2nd Micro layer of PVTE). The electrical resistivity of this layer can be even lower than 1.0 µΩ.cm depends on the thickness of the printed layer.

The described processes above will be the first step of the printing processes on the polyimide film. Hereafter the printing process of thermoelectric material will take place and depend on the design; each zone will be printed and the external connection will be applied. The design and planar geometry of the zone must be harmonized with the planar geometry of the flexible PV sheet.

Figure 6 The silver Nano-wire liquid and electrical conductive film.

1.3.2.4.4   4th Micro layer of PVTE

Manufacturing the polyimide material: The polyimides family is solid substances which are not combustible, not dissolve in organic solvents, oil and acids. But they can be hydrolyzed by alkalis. Polyimide is a polymer of the imide monomers (Figure 7), which can be formed in film/sheet and be used for different application. One of the advantages with these kind films is their heat resistance. The Polyimides do not change the physical form under temperature gradient. As these materials are heat resistance the heat conductivity of the material is low and laying between 0.2 W/(m·K) to 0,6 W/(m.K). But by using the micro thickness layer the matter of heat resistance of the polyimide films will become secondary for TE-layer. Polyimides have an amorphous structure and at 20 ^{o}C room temperature have a density of 1400 - 1500 mg/cm^2. Polyimides materials are produced mainly by poly condensation of the tetra carboxylic acids and also their derivatives. In this process first the macromolecular soluble polyamic acids are produced and later on thin and thick film material and fibers are formed from polyamic acids. After this process the materials will be treated by heat. Polyimides are also worked by pressure moldings. There are different applications where the Polyimides beneficially can be applied. One of the important advantages of polyimide is the resistivity to the fast electron, Ozone and the radiations from the sun, which will be dominant by using the transparent Photovoltaic substrate. The resistivity to the fast electron make it possible to produce high voltage layers, where the voltage output from TE-layer will be designed according to the voltage output of a photovoltaic sheet layer, where the surface area is similar to the thermoelectric sheet layer. By this way one of the challenges to convert the output voltage to a high voltage for matching the voltage of the PV sheet layer will be ignored. Important data about this process material is mentioned in the Table 3.
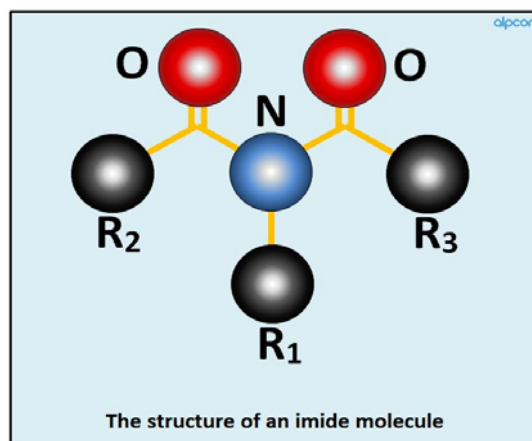

Figure 7 Structure of an imide molecule.

Table 3 Important data of the process material.

Description	Value	Unit
Tensile strength at 20oC	180	MN/m2
Thermal conductivity	0.52	W/(m·K)
Melting point	none	-
Density at 20oC	1430	kg/m3
Impact test/Notch test	4−8	kJ/m
Vicat softening level	After 225	oC
Thermal expansion coefficient	$5.5 \times 10-5$	Per K
Specific heat capacity	1.15	kJ/(kg·K)
Dielectric constant	3.5	at 1 MHz
Water absorption	0.32	(ASTM)

Supplying commercially polyimides film sheet: There are numerous suppliers which supply this material. The material is modified for different application. Some of the Polyimides film structure have tendency to electrostatic charge on the surface especially in present of air-flow. They can release over 9.000 Volts discharge to the components and circuit boards which are in contact to them. This electro discharge can damage the sensitive electronic, especially when a device contains programmable chips and is not earth protected. There are also made many other industrial formulas to avoid such a disadvantage of polyimides films. The recent researches and excellent high technological industrial methods made it possible for researchers to make a polyimide film (Figure 8) with very low electrostatic charge at un-wind environments. The new films overcome this problem without any of the typical draw-backs of conventional anti-static/static-free films materials. Even this kind film is now available with both polyethylene and cardboard tape core. The new polyimide films are used for PCB solder masking and high temperature application. This kind film cannot change the phase and be soften when the temperature raise, thus the film provides an excellent release surface at elevated temperatures.

An efficient flexible TEG require that the fabrication gives possibility for a high density thermoelectric material with high aspect-ratio TE-legs/points placed and contacted electrically in series. By utilizing a flexible device design it will be possible to fabricate the TEG on polyimide flexible film which is very suitable insulating substrate for higher electrical voltages. Furthermore a deposition technique of the printing on the film meets the requirements for fabrication of flexible and planar TEG devices.

The process of dispenser printing involves the deposition of a synthesized thermoelectric ink. This ink can consist of different active materials in a polymer binder which normally can be formulated by silicon family and solvents. At this step the important factor is to optimizing and synthesizing an effective thermoelectric composite for printing process. One of the commercially available film materials is Kapton HN with a relevant data in the Table 4.
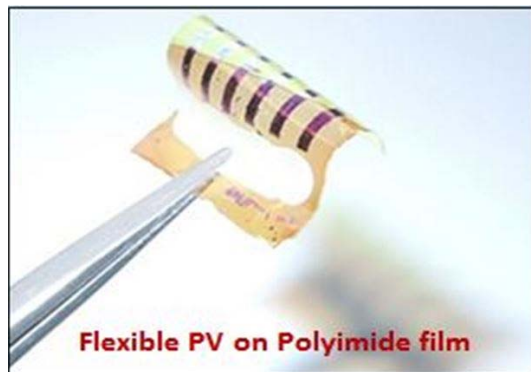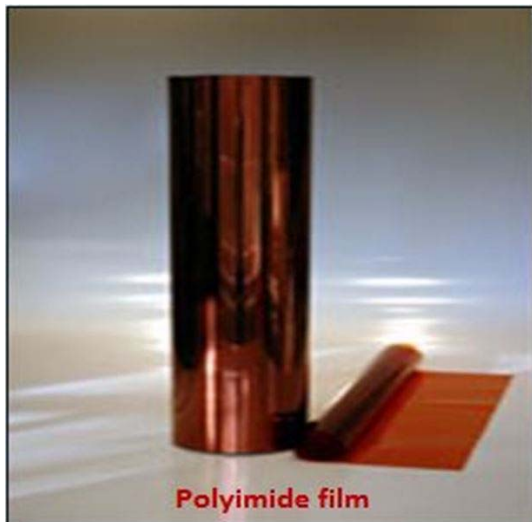
Figure 8 The same Polyimide films for flexible PV and TEG.

Table 4 A commercially available film materials is Kapton HN.

SPECS	
ITEM	Film Tape
TYPE	Premium Grade, No Adhesive
MATERIAL	Dupont Kapton Polyimide
THICKNESS	5.0 mil
WIDTH	5"
LENGTH	50 ft.
COLOR	Amber
PERFORMANCE TEMP.	-452 Degrees to 752 Degrees F
STANDARDS	ASTM D5213
UNSPSC	31201522
WEIGHT	0.960000
SKUS	3ZVN6

1.3.2.4.5   5th Micro layer of TVTE

This layer is exactly the same material as the 1st layer. The bonding layer is thin and thermal conductive silicon substance. The micro channel heat exchanger will be bonded to this layer for cooling of the flexible TE device. As mentioned in description for coating of 1st micro layer, the coating will be applied to the surfaces between PV substrate/layer and the TE-substrate/layer, furthermore between the TE-layer and the micro channels surface. The direct bonding process gives very good flexibility for the new sandwich device and its layers. Here we must take in account that the radio of the multi sandwich device flexibility is used when the micro channel heat exchanger will be designed as a flexible device, or as a device with not planar surface. The radio of the total sandwich device flexibility is zero when the micro channel heat exchanger is designed as a planar solid state device. The silicone bonding material layers which must be used for this purpose have an adhesion to steel is measured which is about 1.2 kg/cm^2, which make it possible for mounting of the device in any position without using the clamping tools.
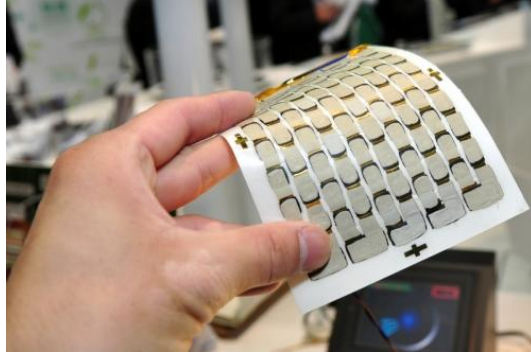
Figure 9 Flexible PVTEG device.

1.3.3 Selected results

1.3.3.1 Micro-structured heat sinks for TEG

Figure 10 shows configuration of the heat sinks with the TEG, indicating the symmetric calculation domain that is a quarter of the TEG and heat sinks. In this numerical investigation, the length of the studied thermoelements is $2\,\text{mm}$ with squared footprint area of $1\,\text{mm}^2$. The distance between the thermoelements is $0.8\,\text{mm}$. The thickness of the ceramic substrate and the silver interconnectors are $0.07\,\text{mm}$ and $0.1\,\text{mm}$, respectively. For better consideration of the effect of flow and heat transfer in the heat sink on the power generation in the TEG, the properties of thermoelements are taken constant in this study. The thermoelectric materials are Bismuth Telluride (Bi_2Te_3) with electrical resistivity and Seebeck coefficient equal to $9.09\,\Omega.\text{m}$ and ±0.2 mV/K, respectively. Thermal conductivity of the thermoelements affects the heat flux across the TEG module and the power generation. Therefore, three values for thermal conductivity of the thermoelements are considered, $0.8\,\text{W/m}.\text{K}$ [24, 25], $1.6\,\text{W/m}.\text{K}$ [26], and $2.0\,\text{W/m}.\text{K}$ [27]. The ceramic substrate is Alumina ($\text{AD}-995, \text{Nom}.\,99.5\%\,\text{Al}_2\text{O}_3$) with thermal conductivity of $30\,\text{W/K}.\text{m}$. The interconnector is Silver with thermal conductivity of $429\,\text{W/K}.\text{m}$. Linear variation of the interconnector electric resistivity with the temperature is $0.0038\text{T} + 1.52 \times 10^{-8}\,\Omega.\text{m}$ [28]. Water is used as the coolant fluid with the inlet temperature of $290\,\text{K}$. The range of the flow inlet velocity to the microchannels is $0.01 - 0.7$ m/s that produces Reynolds number $3.9 - 276.3$ in the PFHS and $2.2 - 153.5$ in the CCHS. Fixed temperatures considered for the hot junction are $350\,\text{K}$, $450\,\text{K}$ and $550\,\text{K}$. The designed microchannels have the same hydraulic diameter equal to $75\,\mu\text{m}$. Table 5 presents properties of the coolant fluid and the heat sink used in the simulation. Furthermore, Figure 11 illustrates a screen shoot of the software (ANSYS) used to solve the 3-D problem of the coupled thermoelectric and heat sink for a sample thermoelement heat transfer conductivity and PFHS.
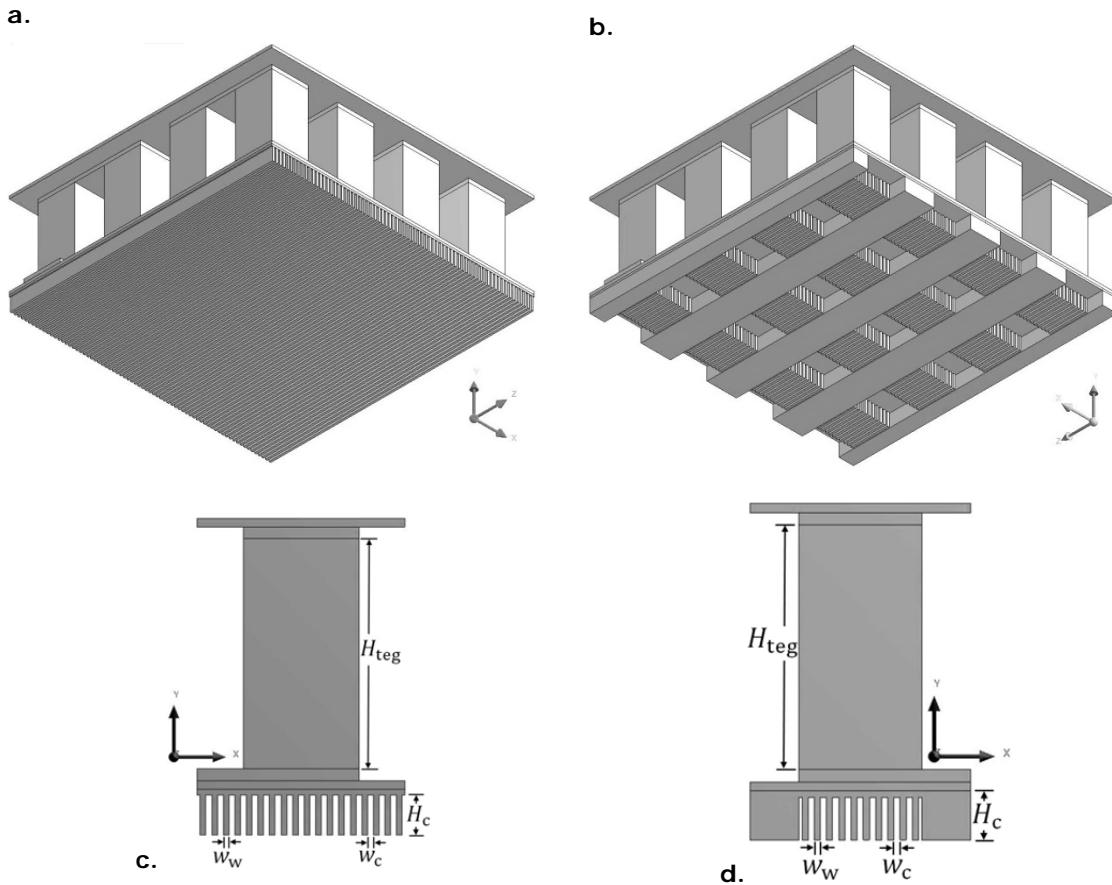
Figure 10 Configuration of the studied TEG and heat sinks a. TEG and PFHS, b. TEG and CCHS, c. front view of symmetric domain of thermoelement and PFHS, d. front view of symmetric domain of thermoelement and CCHS.
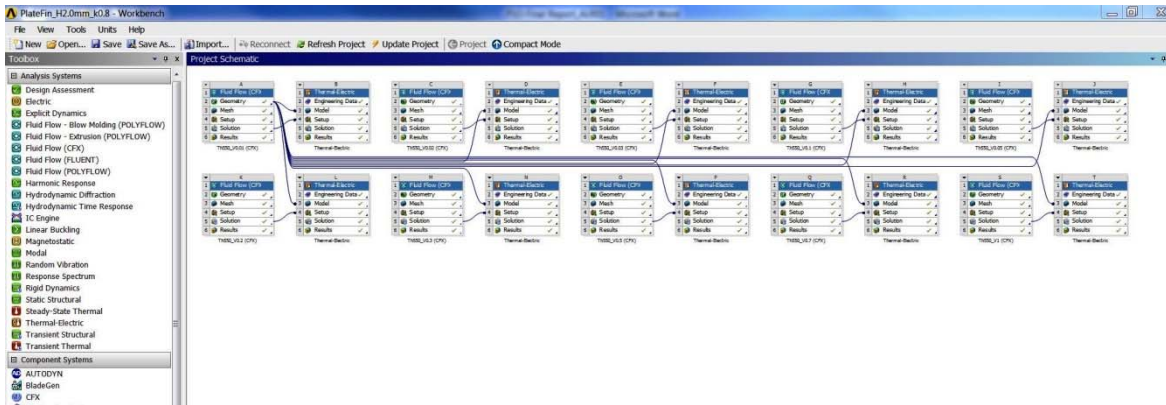

Figure 11 Screen shoot of the ANSYS software used to solve the 3-D problem of the coupled thermoelectric and heat sink.

Table 5 Properties of the coolant fluid and the heat sink.

Dimension	$k_{al}(W/m\,K)$	$k_f(W/m\,K)$	$\rho_f(kg/m^3)$	$\mu_f(kg/m.s)$	$c_f(J/kg.K)$
Value	237	0.6	998.2	0.001	4182

The thermoelectrical characteristic of the thermoelements are implemented in a three dimensional simulation environment and are solved by the finite element method, Mechanical, in conjunction with the computational fluid dynamics (CFD) simulation environment, CFX, that solves the thermal and fluid coupled equations in the heat sinks and in the coolant fluid.

To reduce the computational effort, a symmetry boundary condition is imposed, which surrounds a quarter of the TEG and the heat sinks.

The aim of computational model used in this study is to demonstrate detailed results for 3D temperature distribution and voltage generation in the TEG affected by the flow in the micro-structured heat sinks. The application of the heat sinks provides realistic thermal boundary condition in the TEG in contrast to the commonly works on thermoelectricity, where the cold junction is at constant temperature. The flow temperature rises along the heat sink due to absorbing heat. Therefore, temperature on the cold junction of the thermoelements is not constant, and each thermoelement generates different voltage. However the electric potential increases in the series design of the n and p-type thermoelement, as is illustrated in Figure 12 The effect of flow temperature variation on the temperature distribution in the thermoelements can be seen in Figure 13 This effect is more visible at low flow velocity due to rapidly increase of the flow temperature along the heat sink. For better comparison, Table 6 shows the voltage generation in the thermoelements for sample inlet velocities.
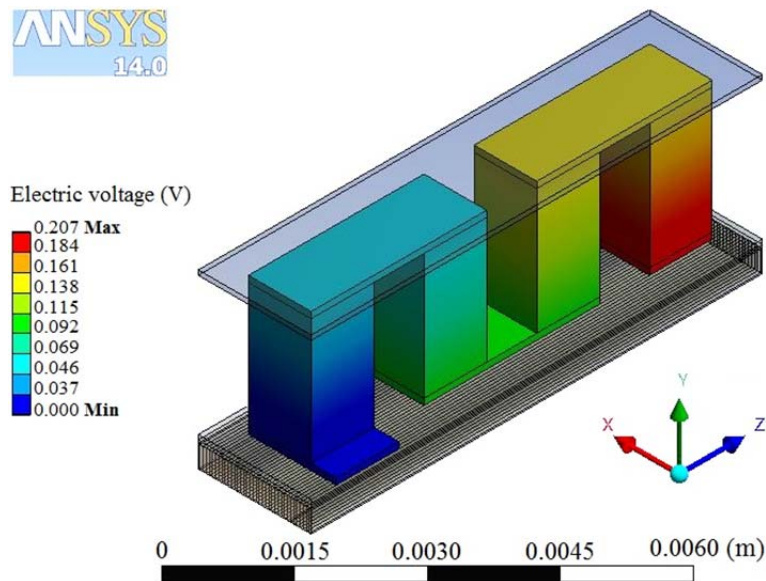

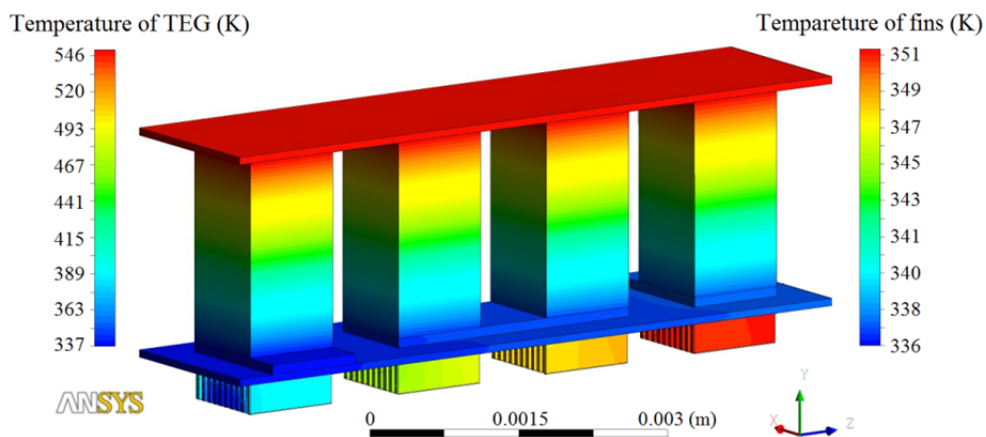*Figure 12 Generation of the electric voltage, $v_i = 0.5\ m/s\ T_h = 550\ K,\ k_{teg} = 1.6\ W/m.K.$*

Figure 13 Temperature distribution in the TEG and fins of CCHS, $v_i = 0.01\ m/s\ T_h = 550\ K,$
$k_{teg} = 1.6\ W/m.K.$

Table 6 *Voltage generation in the thermoelements for sample inlet velocities, $T_h = 550\,K$, $k_{teg} = 1.6\,W/m.K$.*

v_i(m/s)	voltage generation in TEG with CCHS (V)				voltage generation in TEG with PFHS (V)			
	TE#1	TE#2	TE#3	TE#4	TE#1	TE#2	TE#3	TE#4
0.01	0,04542	0,04462	0,04428	0,04401	0,04765	0,04680	0,04634	0,04599
0.10	0,05131	0,05103	0,05085	0,05067	0,05162	0,05144	0,05132	0,05120
0.70	0,05168	0,05163	0,05160	0,05156	0,05176	0,05172	0,05171	0,05168

At higher flow rate condition, the thermal performance of the PFHS is slightly superior to the CCHS. As discussed by Kim et al. [29], for small dimensionless required pumping power, $\log(P_{pump}/(\mu^3/(\rho^2 D_{h,fr})))$, and large dimensionless heat sink length, $\log(H_c/D_{h,fr})$, the PFHS is recommended. For the considered inlet velocity in this study, the dimensionless required pumping power is smaller than 11.35 for dimensionless heat sink length equal to 1.03, where the FPHS is recommended. Moreover, at low flow rate the PFHS shows much better performance than the CCHS.

Microchannel heat sinks contain several channels in contrast to typical heat sinks with large scale channels which make it difficult to achieve constant wall temperature or constant wall heat flux. Therefore, conjugate heat transfer effect should be accounted for the microchannel heat exchangers, particularly at low Reynolds number [30]. As is mentioned in previous works [31, 32] and as Figure 13 reveals in this study, the heat distributes in the part of the CCHS that no fin is designed. Therefore, thermal performance of the CCHS drops at the low flow inlet velocity and power generation in the TEG is less than that with PFHS. Since water is considered as the coolant fluid in this study, the temperature variation of the cold junction is limited in a small range of temperature. However suitable temperature is available on the cold junction due to relatively high specific heat capacity of the water. Therefore, as Figure 14 shows, the voltage generation does not drop sharply when the flow inlet velocity decreases. However, the effect of the hot junction temperature dominates in voltage generation and the power generation is strongly affected by temperature difference of the cold and hot junctions.
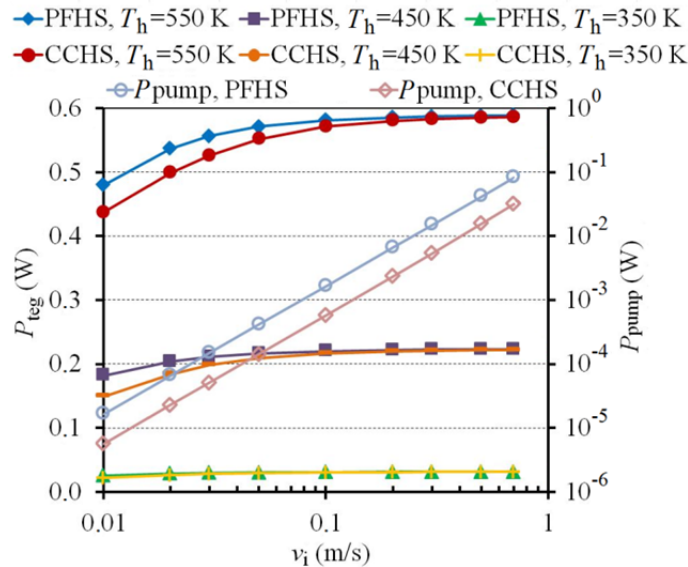

Figure 14 *Variation of electric voltage generation and required pumping power with flow inlet velocity, $k_{teg} = 1.6\ W/m.K$.*

When the system operates at high inlet velocity and low temperature difference, the net power of the system can be minus due to high required pumping power and small power

generation. Therefore as Figure 15 reveals, depending to the design of the heat sink, the limitation of inlet velocity needs to be considered to avoid of minus net power. On the other hand, with decrease of the inlet velocity the power generation reduces, however a smaller pumping power is required due to lower pressure drop in the heat sink. In addition, to avoid of vaporization of the coolant fluid, there is a lower limit for the flow inlet velocity. In between of the low and high limitations of the flow inlet velocity there is an optimal point for each hot junction temperature and type of heat sink that makes maximum net power in the TEG. When the hot junction temperature increases the maximum net power occurs at higher flow inlet velocity, because the increase of the voltage generation is greater for higher hot junction temperature compared to that for small hot junction temperature.
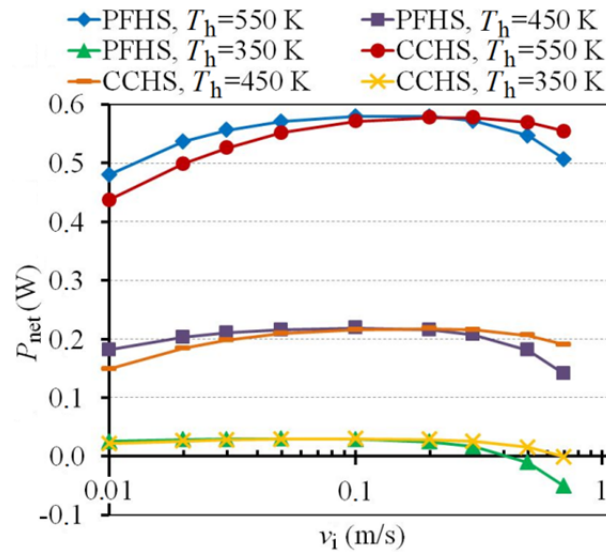

Figure 15 Variation of thermoelectric net power with flow inlet velocity, $k_{teg} = 1.6 \, W/m.K$.

Researchers in the field of thermoelectrics have been tried to minimize thermal conductivity of the thermoelectric materials in order to provide higher temperature difference and to enhance power generation in TEGs. However, the effect of thermal conductivity needs to be considered in conjunction with the heat sink. As Figure 16 shows, the thermal conductivity does not have strong influence on maximum value of the net power and the maximum net power is slightly superior for smaller thermal conductivity materials. However, applying smaller thermal conductivity material makes advantages of providing the maximum net power at lower inlet velocity and smaller pumping power.

Over studied range of the flow inlet velocity, the heat transfer rate in the PFHS is higher compared to the CCHS and it makes higher heat flux across the TEG (Figure 16). For constant hot junction temperature and thermal conductivity of thermoelectric materials, the higher heat flux creates higher temperature difference in the TEG and enhances the voltage generation. Although the required pumping power is smaller in the CCHS, the overall net power in the TEG with PFHS is slightly superior to that with CCHS. It should be noted that this evaluation is based on the particular considered microchannel dimensions, type of coolant fluid and boundary conditions.
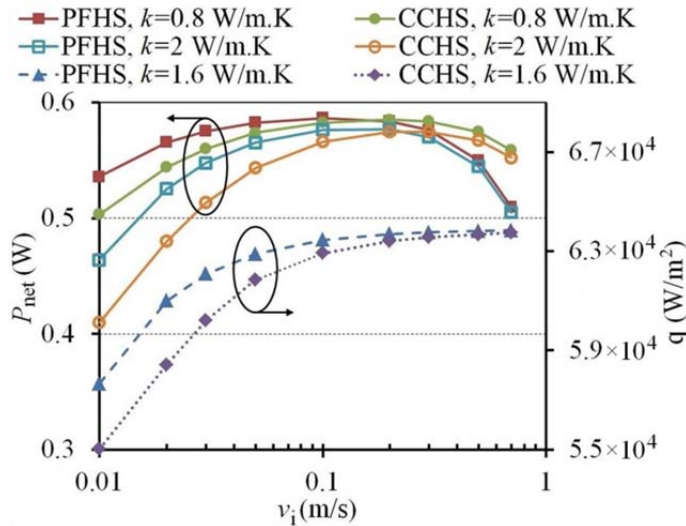
Figure 16 Variation of thermoelectric net power and heat flux across the TEG with flow inlet velocity, $T_h = 550\,K$.

1.3.3.2 Integrated PV and TEG

Appendix B describes in detail the developed model for PVTEG integrated model. The modeling of the PV-only and PVTEG is based on practical variable parameters. The results of the models are a function of solar radiation, ambient temperature wind speed, fill factor of the TEG (f) and figure of merit of thermoelectric materials (ZT). Furthermore, two special cases are also considered to evaluate the PVTEG model where the back surface of the PVTEG is isolated and an active cooling principle enhances heat transfer coefficient on the rear surface of PVTEG. When the PVTEG module is installed on roof of building with small roof-module distance we can suppose that heat transfer coefficient on the rear surface is low ($H_{wc} \approx 0$). For force convection by air the heat transfer coefficient varies $20 - 50\ W/m^2K$, while this range is $300 - 1000\ W/m^2K$ for water. Table 7 shows the values of variable parameters in this project that consider over wide range of weather conditions. Among the considered variables $G_t = 1000\ (W/m^2)$, $T_a = 285\ (K)$, $V_m = 5\ (m/s)$, $f = 0.6$ and $ZT = 1$ are taken at reference variables. When effects of one or some variables are discussed in this project, the other variables are fixed at the reference values.

Table 7 Variable parameters of the weather condition and TEG applied in this project.

Parameters	Values
$G_t\ (W/m^2)$	500, 800, 1000, 2000, 5000, 10000
$T_a\ (K)$	270, 275, 280, 285, 290, 295, 300
$V_m\ (m/s)$	1, 5, 10, 15, 20, 25, 30
f	0.1, 0.2, 0.3, 0.4, 0.5, 0.6, 0.7, 0.8, 0.9
ZT	1, 2, 3, 4
$H_{wc}\ (W/m^2K)$	50, 100, 200, 500, 1000, 2000, 5000, 10000

Power generation in the TEG strongly depends on the temperature difference between the cold and hot junction of the thermoelements. As (16) shows, a higher temperature difference makes the TEG more efficient and enhances power generation in the TEG. The impact of heat transfer coefficient on the rear surface of the PVTEG is small at low wind speed and cannot make suitable temperature difference between two junctions of the TEG. Therefore, the power generation by the TEG is too small. The heat transfer coefficient on the rear surface increases with the wind speed and the power generation in the TEG enhances. The power generation by the TEG decreases at high wind speed. High heat transfer coefficient on the front surface of the glass cover decrease the temperature at the hot junction of the TEG and re-

duces the power generation. However, as Figure 17 shows, the power generation by the TEG is not comparable with the power generation by the PV cell for low ZT. Power generation by the PV-only and PVTEG enhance similarly when the wind speed increases.
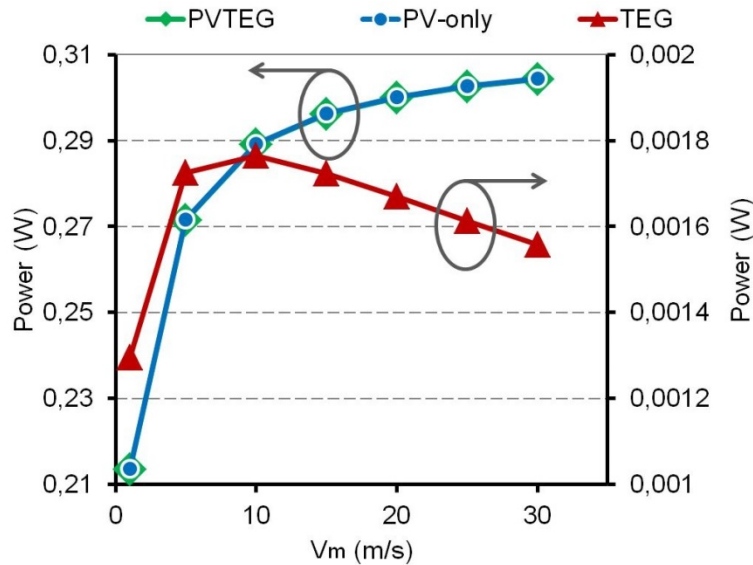
Figure 17 Variation of the power generation by TEG, PV-Only and PVTEG with wind speed.

The temperature difference between the junctions of TEG can be modified by fill factor in the TEG which is ratio of the thermoelements area per area of the TEG module. With increase of the fill factor, thermal resistance of the TEG decreases and higher amount of heat flux passes across the TEG. On the other hand, the temperature difference in the TEG decreases and reduces the efficiency of the TEG. Considering both of these effects, the results of Figure 18 illustrates that power generation in the TEG decreases when the fill factor increases. Apart from the TEG power generation, when the heat flux across the TEG enhances, the temperature of the PV cell in the PVTEG model reduces which results a higher power generation by the PV cell. In general, the power generation in the PVTEG increases with the fill factor. However, this value is still lower than power generation by the PV-only.

Figure 18 Variation of the efficiency of TEG, PV-Only and PVTEG with fill factor.

The most suitable thermoelectric materials for the temperature range in the TEG are bismuth-telluride based materials [33] which have a ZT < 1. Therefore, for current thermoelec-

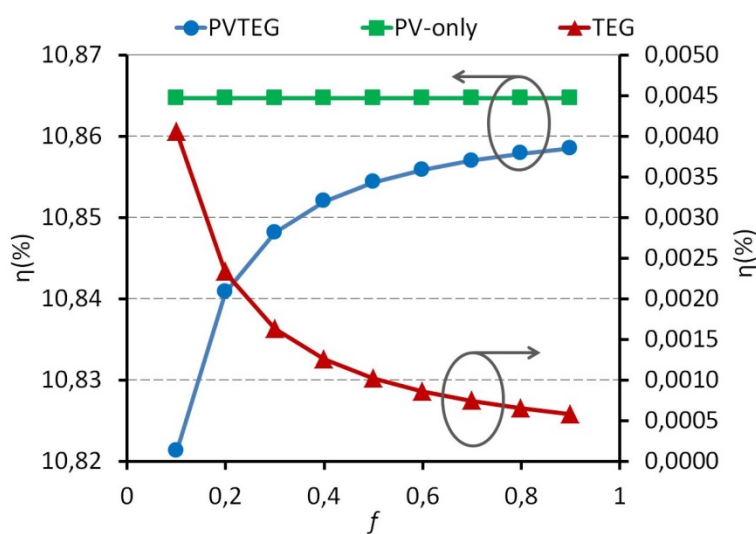tric materials applying the TEG module to the PV cell may cause to reduce the overall electrical conversion efficiency and may not be reasonable. If development of thermoelectric materials can provide higher ZT in future, then a hybrid module of the PVTEG can enhance the total efficiency, as can be seen in the Figure 19.
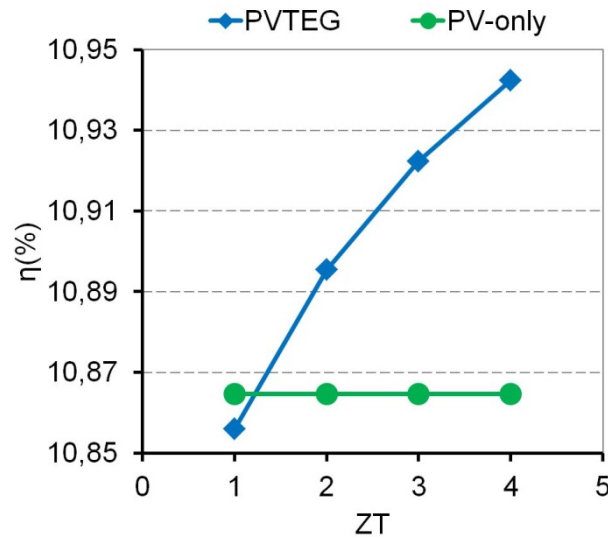
Figure 19 Variation of the efficiency of PV-Only and PVTEG with thermoelectric figure of merit.

Figure 20 shows variation of the radiative heat loss and the efficiency over a wide range of heat transfer coefficient on the rear surface of the PVTEG. Higher heat transfer on the rear surface affects the temperature distribution in the modules and reduces temperature on the PV cell. According to (16), the radiative heat loss decreases as the temperature variation between the PV cell and sky reduces. Since the temperature of the PV cell of the PVTEG is higher than that of PV-only surface due to additional thermal resistance caused by applying TEG, radiative heat loss from the PV-only cell is lower compared to the PVTEG. Reduction of the radiative loss also means that a bigger portion of the solar radiation is converted into electricity and the efficiency of the modules increases. Moreover as mentioned, when the surface temperature of the PV cell decreases its efficiency increases. Therefore, a higher heat transfer on the rear surface of the PVTEG leads to a higher efficiency.
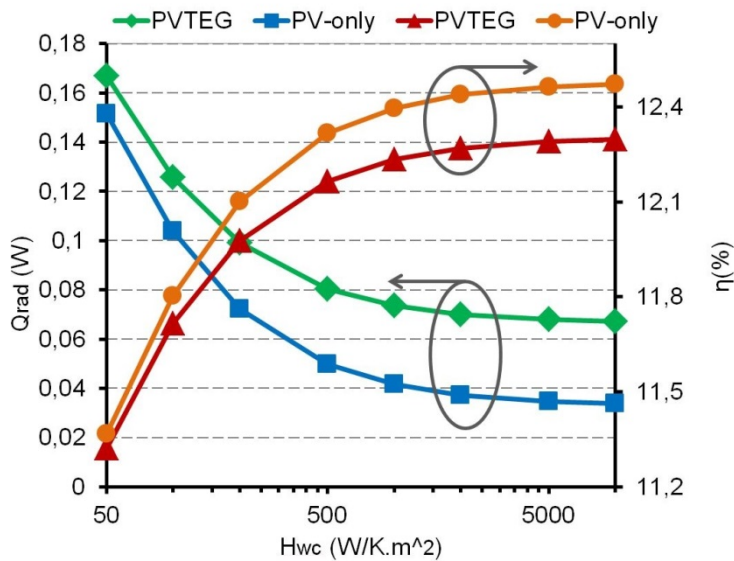
Figure 20 Variation of the radiative heat loss and PVTEG efficiency with heat transfer coefficient on the rear surface

As mentioned, efficiency of the PVTEG can enhance with higher ZT of thermoelectric materials and heat transfer coefficient on the rear surface. A 3-D view of the efficiency variation as shown in Figure 21 can show the limitation of the efficiency enhancement for the considered variables. The active cooling requires cooling power dependent to the volumetric coolant flow and pressure drop in the heat sink that reduces net power generation. In case of applying active cooling principle the cost of cooling energy needs to be evaluated.

For the special case which the rear surface of the PVTEG is assumed insulated in order to simulate roof installation of the PVTEG with small roof-module distance, the temperature difference between the two junctions of the TEG is zero because of zero value of heat transfer coefficient on the PVTEG rear surface. Therefore, the power generation by the TEG is zero.
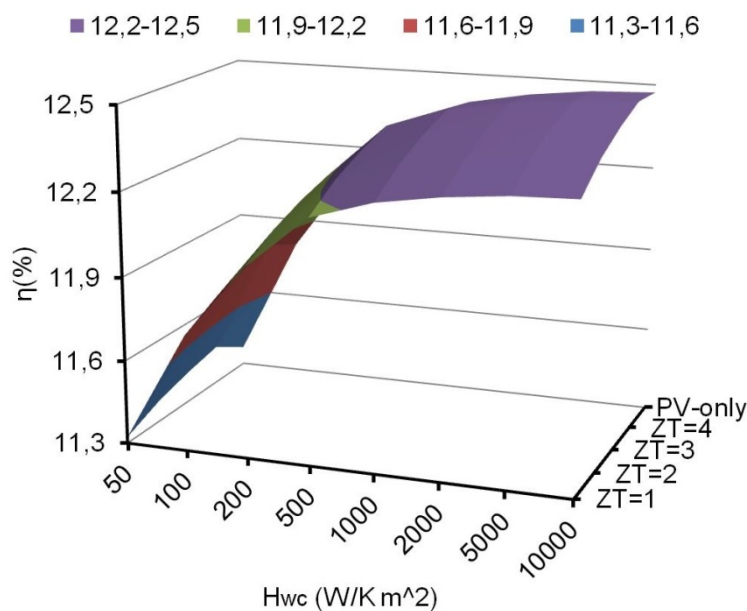
Figure 21 Variation of the efficiency of PVTEG efficiency with heat transfer coefficient on the rear surface and thermoelectric figure of merit.

1.4 Utilization of project results

The results of this project will be published in high impact international journals. The first journal paper will present a numerical comparison of micro-structured flat-plate and cross-cut heat sinks applied to thermoelectric generators (Appendix A). The results of the hybrid model for photovoltaic cell and thermoelectric generator will be developed with adding results for historical weather conditions in sample cities in Europe (Aalborg in Denmark and Malaga in Spain). This journal paper, that proposes comprehensive and coupled model, presents detail information of the PVTEG module in real weather condition. Both of these topics are shared in the International Conference on Thermoelectrics (ICT). The results of numerical investigation were presented in ICT 2013, Kobe, Japan and the hybrid model is presented in ICT 2014, Nashville, TN, USA. The methodology representing technology of the flexible PV-TEG module has a great potential as future proposal. This methodology offers a unique technology that is able to expand research at Department of Energy Technology at Aalborg University. However to submit this methodology as a patent or to consider it as future research activity, further issues about applied materials need to be carefully considered.

1.5   Project conclusion and perspective

The configuration effects of PFHS and CCHS on the power generation, the required pumping power and the net power are compared in this project over a wide range of flow inlet velocity. The 3D governing equations of thermoelectricity and flow are solved, and analysis of the model generates detailed description of the temperature distribution, voltage generation, required pumping power and the net power in the TEG through realistic thermal boundary conditions. The results illustrates that each thermoelement generates individual voltage due to effect of flow temperature variation along the heat sink. In between of the low and high limitations of the flow inlet velocity there is an optimal point for each hot junction temperature and type of heat sink that the thermoelectric net power in the module is the maximum. The results also show that, the maximum net power occurs at lower flow inlet velocity when the hot junction temperature decreases and when the thermal conductivity of the thermoelements is smaller. Thermal conductivity of thermoelectric materials does not have strong influence on maximum power generation for the considered heat sink geometries. The CCHS requires smaller pumping power but the overall net power in the TEG with PFHS is slightly superior to that with CCHS.

In addition, a coupled model of hybrid photovoltaic and thermoelectric generator is developed in this study and the results are compared with a PV cell to show the performance of the hybrid model. The studied modules include practical and effective parameters of weather condition and thermoelectric generator module. 1-D temperature distribution, electric power generation in the thermoelectric generator and photovoltaic cell are obtained through a nonlinear set of equations and over a wide range of the variable parameters. The results illustrate that conversion efficiency of the hybrid PVTEG with ZT=1 is less than conversion efficiency of the PV-only. However, if development of thermoelectricity can provide higher ZT materials in future, a hybrid module of the PVTEG can enhance the total efficiency compared to the PV-only case. Electrical power generation in the TEG decreases when the fill factor increases while the power generation in the PVTEG increases with the fill factor. For case of roof installation of the PVTEG with small roof-module distance, power generation by the TEG is zero because of zero value of temperature difference between the two junctions of TEG.

As mentioned, the results of this project show that a hybrid module of PVTEG cannot improve the total efficiency compared to the PV-only cell. Therefore, this project will not focus on the integration of the conventional PV cells and TEGs for future work. The results of the hybrid model also show that, when the solar radiation is concentrated on the PV cell, the PVTEG module has better performance compared to the PV-only cell because higher heat flux across the TEG and temperature difference between the cold and hot junctions is available. Therefore, integration of CPV with TEGs can offer a promising offer to increase efficiency of harvesting solar radiation. The concentrated level can be up to 1000 suns with consideration of temperature limitation on the CPV cell and in the TEG module. When this project consortium have shared the results of this project in the ICT conferences with other active institutes in the field of thermoelectricity and photovoltaics in Denmark and Europe to invite them to collaborate for project proposals on hybrid CPV and TEG systems, feedbacks on this idea were remarkable and there are great interests to join to the project association for further research activities considering CPV-TEG.

1.6   Updating Financial Appendix and submitting the final report

The Financial report of this project is already submitted to Ms. Inger Pihl Byriel (E-mail: ipb@energinet.dk). Moreover, the Financial Appendix (Appendix C1 and Appendix C2) is attached with this project report as well.

References

[1] A. Rezania, L.A. Rosendahl, H. Yin, Parametric optimization of thermoelectric elements footprint for maximum power generation, Journal of Power Sources 255 (2014) 151-156.

[2] E.M. Dede, Y. Liu, Experimental and numerical investigation of a multi-pass branching microchannel heat sink, Applied Thermal Engineering 55 (2013) 51-60.

[3] M. Reyes, J.R. Arias, A. Velazquez, J.M. Vega, Experimental study of heat transfer and pressure drop in micro-channel based heat sinks with tip clearance, Applied Thermal Engineering 31 (2011) 887-893.

[4] A. Rezania, L.A. Rosendahl, S.J. Andreasen, Experimental investigation of thermoelectric power generation versus coolant pumping power in a microchannel heat sink, International Communications in Heat and Mass Transfer 39 (2012) 1054-1058.

[5] A. Rezania, K. Yazawa, L.A. Rosendahl, A. Shakouri, Co-optimized design of microchannel heat exchangers and thermoelectric generators, International Journal of Thermal Sciences 72 (2013) 73-81.

[6] Yu. Vorobiev, J. Gonza´lez-Herna´ndez, P. Vorobiev, L. Bulat, Thermal-photovoltaic solar hybrid system for efficient solar energy conversion, Solar Energy 80 (2006) 170-176.

[7] A. Muhtaroglu, A. Yokochi, A. von Jouanne, Integration of thermoelectrics and photovoltaics as auxiliary power sources in mobile computing applications Journal of Power Sources 177 (2008) 239-246.

[8] Hybrid power systems, www.redhawkenergy.net.

[9] Micropelt thin film thermoelectrics, www.micropelt.com

[10] E.A. Cha´vez-Urbiola, Yu.V. Vorobiev, L.P. Bulat, Solar hybrid systems with thermoelectric generators, Solar Energy 86 (2012) 369-378.

[11] M. Mizoshiri, M. Mikami, K. Ozaki, Thermal–photovoltaic hybrid solar generator using thin-film thermoelectric modules, Japanese Journal of Applied Physics 51 (2012) 06FL07, 1-5.

[12] N. Wang, L. Han, H. He, N.H. Parkb K. Koumoto, A novel high-performance photovoltaic–thermoelectric hybrid device, Energy Environ. Sci. 4, (2011) 3676-3679.

[13] L.D. Landau, E.M. Lifshitz, Electrodynamics of continuous media, 2nd Edition, Butterworth-Heinemann, Oxford (1984).

[14] E.E. Antonova, D.C. Looman, Finite elements for thermoelectric device analysis in ANSYS, 24th International Conference on Thermoelectrics (2005) 215- 218.

[15] F.J. Lesage, É.V. Sempels, N. Lalande-Bertrand, A study on heat transfer enhancement using flow channel inserts for thermoelectric power generation, Energy Conversion and Management 75 (2013) 532-541.

[16] M.I. Hasan, Investigation of flow and heat transfer characteristics in micro pin fin heat sink with nanofluid, Applied Thermal Engineering 63 (2014) 598-607.

[17] G. Notton, C. Cristofari, M. Mattei, P. Poggi, Modelling of a double-glass photovoltaic module using finite differences. Applied Thermal Engineering 25 (2005) 2854–2877.

[18] D.L. Evans, Simplified method for predicting photovoltaic array output. Solar Energy 27 (1981) 555–560.

[19] E. Skoplaki, J.A. Palyvos, On the temperature dependence of photovoltaic module electrical performance: A review of efficiency/power correlations, Solar Energy 83 (2009) 614–624.

[20] D.L. Evans, L.W. Florschuetz, Terrestrial concentrating photovoltaic power system studies. Solar Energy 20 (1978) 37–43.

[21] J.A. Palyvos, A survey of wind convection coefficient correlations for building envelope energy systems' modeling, Applied Thermal Engineering 28 (2008) 801–808.

[22] W.H. McAdams, Heat Transmission, third ed., McGraw-Hill Kogakusha, Tokyo, Japan, 1954, p. 249.

[23] L.L. Baranowski, G.J. Snyder, and E.S. Toberer, Effective thermal conductivity in thermoelectric materials, J. Appl. Phys. 113 (2013) 204904.

[24] J.J. Shen, Z.Z. Yin, S.H. Yang, C. Yu, T.J. Zhu, X.B. Zhao, Improved thermoelectric performance of p-type bismuth antimony telluride bulk alloys prepared by hot forging, Journal of Electronic Materials, 40 (2011) 1095-1099.

[25] L.P. Hu, X.H. Liu, H.H. Xie, J.J. Shen, T.J. Zhu, X.B. Zhao, Improving thermoelectric properties of n-type bismuth–telluride-based alloys by deformation-induced lattice defects and texture enhancement, Acta Materialia 60 (2012) 4431-4437.

[26] J.P. Fleurial, L. Gailliard, R. Tribouler, H. Scherrer, S. Scherrer, Thermal properties of high quality single crystals of bismuth telluride-part i: experimental characterization, Journal of Physics and Chemistry of Solids, 49 (1988) 1237-1247.

[27] S. Ganguly, C. Zhou, D. Morelli, J. Sakamoto, C. Uher, S.L. Brock, Synthesis and evaluation of lead telluride/bismuth antimony telluride nanocomposites for thermoelectric applications, Journal of Solid State Chemistry 184 (2011) 3195-3201.

[28] R.A. Serway, Principles of Physics, 2nd ed., Fort Worth, Texas; London: Saunders College Publishing (1998) 602.

[29] T.Y. Kim, S.J. Kim, Fluid flow and heat transfer characteristics of cross-cut heat sinks, International Journal of Heat and Mass Transfer 52 (2009) 5358-5370.

[30] M. Chen, L.A. Rosendahl, T. Condra, A three-dimensional numerical model of thermoelectric generators in fluid power systems, International Journal of Heat and Mass Transfer 54 (2011) 345-355.

[31] A. Rezania, L.A. Rosendahl, New configurations of micro plate-fin heat sink to reduce coolant pumping power, Journal of Electronic Materials 41 (2012) 1298-1304.

[32] Shan Yin, King Jet Tseng, Jiyun Zhao, Design of AlN-based micro-channel heat sink in direct bond copper for power electronics packaging, Applied Thermal Engineering 52 (2013) 120-129.

[33] G.J. Snyder, E.S. Toberer, Complex thermoelectric materials, Nature Materials, 7 February (2008).

Appendix A

Manuscript 1

A comparison of micro-structured flat-plate and cross-cut heat sinks for thermoelectric generators

A. Rezania, L.A. Rosendahl

A comparison of micro-structured flat-plate and cross-cut heat sinks for thermoelectric generators

A. Rezania[*], L.A. Rosendahl

Department of Energy Technology, Aalborg University, DK-9220 Aalborg, Denmark

Abstract

The configuration of heat sink has a strong influence on the power generation and net power in thermoelectric generators (TEGs). In this study, a micro-structured plate-fin heat sink (PFHS) is compared to a modified design of cross-cut heat sink (CCHS) applied to the TEG. The Power generation in the TEG and the required pumping power in the heat sinks are considered over a range of hot junction temperature and thermal conductivity of the thermoelectric materials. The particular focus of this study is to enhance the net power in the TEG module. The three-dimensional governing equations for the flow and the heat transfer are solved using the computational fluid dynamics (CFD) simulation environment in conjunction with thermoelectric characteristics of the TEG over a wide range of flow inlet velocity. The results, which are in good agreement with the previous studies, show that for a particular type of coolant fluid and dimensions of microchannel the maximum net power in the TEG with PFHS is slightly superior to that with CCHS.

Keywords: *Thermoelectric generator, plate-fin heat sink, cross-cut heat sink, maximum net power.*

1. Introduction

Micro-scale single-phase heat transfer has been widely used in industrial and scientific applications [1]. Using micro-structured heat sinks provides low weight and compact energy system, compared to the conventional types of heat sinks and increases modularity of the power system. This type of heat sink has been interest of researchers for configuration optimization. To decreases the peak temperature and thermal conductance in a microchannel heat sink, Adewumi et al. [2] presented a three-dimension numerical study of an integrated design with micro pin fin inserts.

---

[*] Corresponding author: Alireza Rezania. E-mail: alr@et.aau.dk

Nomenclature

A	footprint area, m^2
$D_{h,fr}$	hydraulic diameter of heat sink frontal area, m
c	specific heat capacity, J/kg.K
H	length, m
J	electric current density, A/m^2
k	thermal conductivity, W/m.K
$\dot{m}$	mass flow rate, kg/s
n	number of uni-couples
Nu	Nusselt number
P	power, W
p	pressure, Pa
Q	absorbed heat, W
q	heat flux across TEG, W/m^2
$\dot{q}$	heat generation rate per unit volume, W/m^3
R	internal electrical resistance, Ω
Re	Reynolds number
T	temperature, K
ΔT	temperature difference, K
$\vec{V}$	velocity vector, m/s
v	velocity, m/s
W	volumetric flow rate, m^3/s
w	width, m
x	distance from channel inlet, m

Greek symbols

α	Seebeck coefficient, V/K
μ	dynamic viscosity, $N.s/m^2$
Π	Peltier coefficient, V
ρ	fluid density, kg/m^3
σ	electrical conductivity, S/m
φ	electric scalar potential, V

Subscripts

al	aluminum
c	channel
cc	cross-cut
f	coolant fluid
h	hot junction
i	inlet
n	n-type thermoelement
net	net
max	maximum
o	outlet
p	p-type thermoelement
pump	pump
teg	thermoelectric generator
w	wall

Beside the thermal resistance consideration, the pressure drop is an important factor for optimization of the micro-structured heat sink design, where the performance of the system depends on the required pumping power [3, 4]. Chai et al. [5] proposed a newly microchannels with periodic expansion–constriction cross section that enhance the average Nusselt number and reduce thermal resistance of the heat sink. Pressure drop in the newly microchannels is lower compared to that in the flat plate microchannels at low Reynolds numbers. The results of a study by Shafeie et al. [6] indicate that for the same required pumping powers, the heat removal of the microchannel heat sink is higher than that in pin finned heat sink at high and medium range of required pumping power ($P_p > 0.5$ W). However in low pumping power, the pin finned heat sink performs slightly better.

Micro-structured heat sinks have been recently applied in the thermoelectric generators (TEGs) [7, 8]. TEGs, which convert heat energy to electrical power by means of semiconductor charge carriers due to temperature difference, have been of great interest to the energy research community in recent years. A key factor in TEG systems is co-optimization of the TEG design with its heat sink, where a challenge is

to design and develop of effective heat exchanger. The maximum power generation in the TEG can be enhanced with applying effective heat sink. For instance, heat transfer coefficient on the cold junction of the TEG can affect the optimal design of the thermoelements, where the maximum power generation occurs at larger ratio of the thermoelements foot print area as the heat transfer coefficient increases [9]. Zhou et al. [10] revealed that parallel flows in the hot and cold heat exchangers lead to greater overall efficiency in the TEG compared to that of the counter flows.

In TEG systems, maximization of net thermoelectric power is more important than enhancement of the power generation. Jang et al. [11] explored optimal fin height of Plate-fin heat sink (PFHS) to maximize the net power density in TEGs. Lesage et al. [12] studied heat transfer enhancement in TEGs using flow channel inserts in the both cold and hot side heat exchangers. Although the pressure drop increases by the tabulating inserts, they showed that the net power generation enhances for a range of temperature difference. The net power generation is defined as power generation by the TEG minus required pumping power in the heat sink.

The temperature distribution in the thermoelements is strongly affected by the flow and heat transfer in the heat sink [13, 14]. Variation of temperature distribution in the heat exchanger causes different temperature distribution in the thermoelements [15]; so that each thermoelement shows particular electrical and thermal behavior, and produces different voltage generation compared to other thermoelements in the module. Higher voltage can be generated in the TEG if the temperature difference of the hot and cold junctions increases by reduction of thermal resistance of the heat sink. One way to reduce the thermal resistance is to enhance the convective heat transfer coefficient by increase of the mass flow rate in the channels. On the other hand, for a given channel hydraulic diameter, when the mass flow rate increases the required pumping power increases due to rapidly increase of the pressure drop in the channel. High mass flow rate may require higher pumping power than the power generation by the TEG and can cause negative net power in the system [16]. The optimal mass flow rate can be explored at a practical limit on the available required pumping power by maximizing power generation in the TEG [7].

Pin-fin heat sink and flat-plate heat sinks (PFHSs) have been widely used in industrial applications due to their advantages. Kim et al. [17] found that to determine the effective type of heat sink between the PFHS and pin-fin heat sink, both of the required pumping power and the length of heat sink should be

considered. Because of advantage of redeveloping region, the pin-fin heat sink can provide high heat transfer rate [18]. On the other hand, the advantages of PFHS are easy fabrication and small pressure drop [19]. At high required pumping power and small length of the heat sink the pin-fin heat sink is recommended, while in small range of pumping power and at large heat sink length the PFHS has better performance. Moreover, it is revealed that, in the middle region of the required pumping power and heat sink length, the cross-cut heat sink (CCHS) is superior depending on its cross-cut length [20].
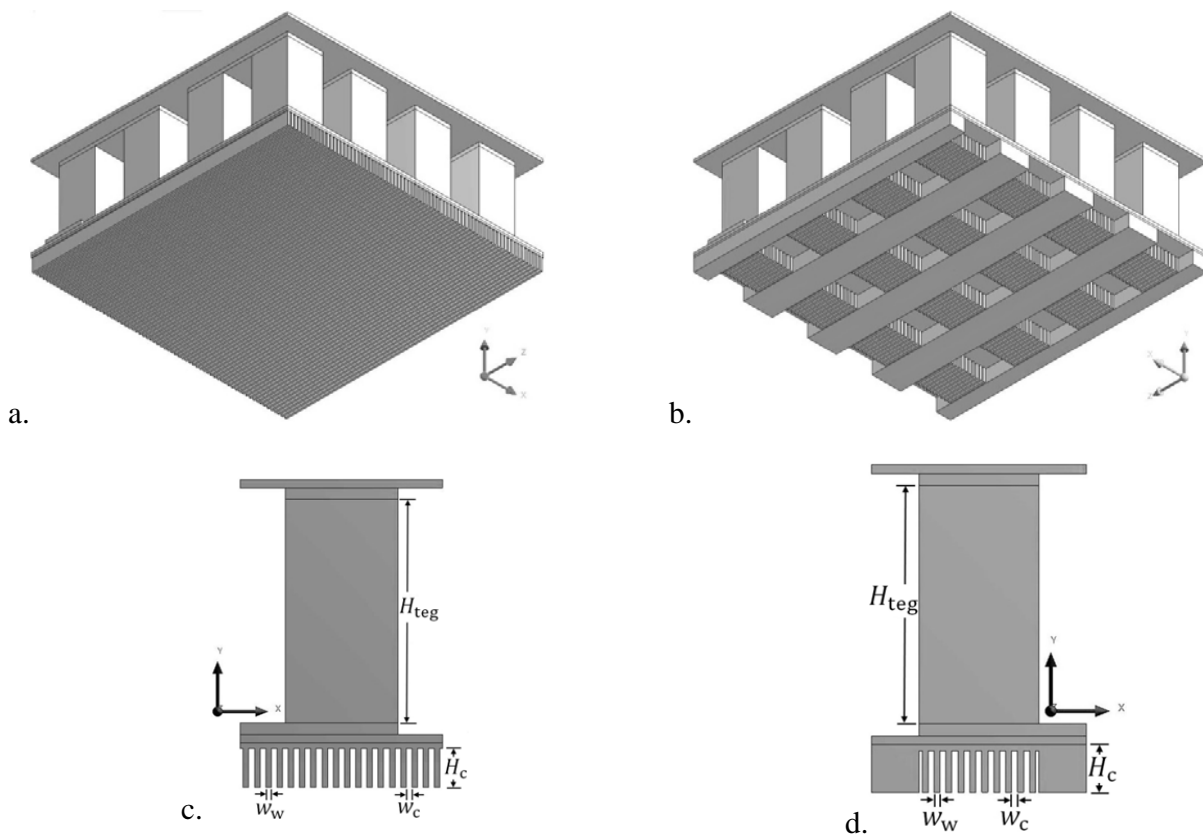
Fig. 1 Configuration of the studied TEG and heat sinks a. TEG and PFHS, b. TEG and CCHS, c. front view of symmetric domain of thermoelement and PFHS, d. front view of symmetric domain of thermoelement and CCHS.

In this study, the effectiveness of a PFHS and a CCHS are compared for reduction of the required pumping power and for maximization of the net power generation. This study is part of an on-going effort to optimize the thermal performance in TEG systems, where new configurations of micro-structured PFHS where recommended [21] to reduce the required coolant pumping power. In contrast

to the previous study, a modified design of the fins under the thermoelements is considered, where this design makes a CCHS for the TEG module. The fluid and thermal characteristics in the heat sinks and the TEG are considered over a wide range of mass flow rate in laminar regime by computational methods. Considering the maximum net power in the system, the required pumping power in the heat sinks is discussed versus the power generation in the TEG for different thermal conductivity of the Bismuth Telluride based thermoelements and imposed hot junction temperatures. Fig. 1 shows configuration of the heat sinks with the TEG, indicating the symmetric calculation domain that is a quarter of the TEG and heat sinks.

2. Governing equations

The effect of radiation and natural convection heat transfer are neglected in this study and the surfaces exposed to the surroundings are assumed to be insulated.

2.1 Thermoelectric generator

Under steady-state condition, the electric field is irrotational and the well-known coupled equations of thermoelectric constitutive [22] including both the heat flow and the continuity of electric charge equations are [23]:

$$\nabla.([\Pi].J) - \nabla.\left([k_{\text{teg}}].\nabla T\right) = \dot{q}, \tag{1}$$

$$\nabla.([\sigma].[\alpha].\nabla T) + \nabla.([\sigma].\nabla \varphi) = 0. \tag{2}$$

The maximum power generation by the TEG occurs at the matched load, where the internal electrical resistance of the uni-couple is equal to the imposed electrical load resistance [12]:

$$P_{\text{teg-max}} = \frac{(\alpha \Delta T)^2}{4R}. \tag{3}$$

The internal resistance of the TEG in (3) is as follows [9]:

$$R = n \times (R_{\text{n}} + R_{\text{p}}) = n \times \left[\left(\sigma_{\text{n}} \frac{A_{\text{n}}}{H_{\text{n}}}\right)^{-1} + \left(\sigma_{\text{p}} \frac{A_{\text{p}}}{H_{\text{p}}}\right)^{-1}\right]. \tag{4}$$

In this study, the length of the studied thermoelements is 2 mm with squared footprint area of $1\ mm^2$. The distance between the thermoelements is 0.8 mm. The thickness of the ceramic substrate and the silver interconnectors are 0.07 mm and 0.1 mm, respectively.

For better consideration of the effect of flow and heat transfer in the heat sink on the power generation in the TEG, the properties of thermoelements are taken constant in this study. The thermoelectric materials are Bismuth Telluride (Bi_2Te_3) with electrical resistivity and Seebeck coefficient equal to $9.09\ \Omega.m$ and ±0.2 mV/K, respectively. Thermal conductivity of the thermoelements affects the heat flux across the TEG module and the power generation. Therefore, three values for thermal conductivity of the thermoelements are considered, $0.8\ W/m.K$ [24, 25], $1.6\ W/m.K$ [26], and $2.0\ W/m.K$ [27]. The ceramic substrate is Alumina ($AD-995, Nom.\ 99.5\%\ Al_2O_3$) with thermal conductivity of $30\ W/K.m$. The interconnector is Silver with thermal conductivity of $429\ W/K.m$. Linear variation of the interconnector electric resistivity with the temperature is $0.0038T + 1.52 \times 10^{-8}\ \Omega.m$ [28].

2.2 Heat sink

To calculate distribution of velocity and temperature for laminar and incompressible flow in the heat sinks the following continuity, momentum and energy equations are solved [29]:

$$\nabla.\vec{V} = 0, \tag{5}$$

$$\rho_f(\vec{V}\nabla.\vec{V}) = -\nabla p + \mu_f\nabla^2\vec{V}, \tag{6}$$

$$\rho_f c_f(\vec{V}.\nabla T) = k_f\nabla^2 T. \tag{7}$$

The rate of heat removal from the heat sink to the coolant flow is:

$$Q = \dot{m}c_f(T_o - T_i). \tag{8}$$

The required pumping power for the flow is related to the pressure drop and the volumetric flow rate in the heat sinks and can be calculated as follows:

$$P_{pump} = \Delta p W. \tag{8}$$

The pressure drop in the heat sink is an important factor that influences net power of the module. The net power supplied by the TEG is the power generation by the TEG minus the required pumping power.

$$P_{\text{net}} = P_{\text{teg}} - P_{\text{pump}}. \tag{9}$$

Water is used as the coolant fluid with the inlet temperature of 290 K. The range of the flow inlet velocity to the microchannels is $0.01 - 0.7$ m/s that produces Reynolds number $3.9 - 276.3$ in the PFHS and $2.2 - 153.5$ in the CCHS. Fixed temperatures considered for the hot junction are 350 K, 450 K and 550 K. The designed microchannels have the same hydraulic diameter equal to 75 μm. Table 1 presents properties of the coolant fluid and the heat sink used in the simulation.

Table 1 Properties of the coolant fluid and the heat sink.

Dimension	$k_{\text{al}}(\text{W/m K})$	$k_{\text{f}}(\text{W/m K})$	$\rho_{\text{f}}(\text{kg/m}^3)$	$\mu_{\text{f}}(\text{kg/m.s})$	$c_{\text{f}}(\text{J/kg.K})$
Value	237	0.6	998.2	0.001	4182

The thermoelectrical characteristic of the thermoelements are implemented in a three dimensional simulation environment and are solved by the finite element method, Mechanical, in conjunction with the computational fluid dynamics (CFD) simulation environment, CFX, that solves the thermal and fluid coupled equations in the heat sinks and in the coolant fluid. To reduce the computational effort, a symmetry boundary condition is imposed, which surrounds a quarter of the TEG and the heat sinks.

3. Validation

For validation, the results in this study are compared to results of previous 3D numerical models.

3.1. Thermoelectric generation

The thermoelectric power generation in this study is compared with a coupled thermoelectric model with 127 uni-couple to the common CFD simulator FLUENT through a user defined function introduced by Chen et al. [30] that is justified by experimental results. The length of thermoelements is 1.6 mm with cross section area of $1.4 \times 1.4 \text{ mm}^2$, and the linear load resistance equal to 3.4 Ω.

Moreover, the power generation in this study is compared with a set of ANSYS couple-field elements [23]. Compared to the previous studies, the maximum difference in power generation is 14.2 %, and it happens at temperature different 40 K. Fig. 2 illustrates good agreement between simulated power generation in this study and the previous studies [23, 30].
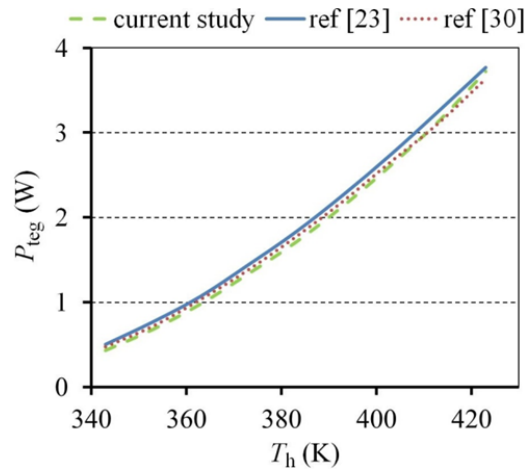
Fig. 2 Comparison of power generation in the TEG module compared to ref [23] and ref [30].

3.2. Heat sinks

The thermal characteristic of the PFHS is validated with the numerical investigation by Chen et al. [31] with the same geometrical details. Fig. 3 shows variation of the circumferential Nusselt number along the PFHSs with the same geometrical details and boundary conditions. Moreover, thermal resistance of the CCHS is compared to results of [20] that consider characteristics of CCHSs. The comparison of the thermal resistance is revealed by Fig. 3 over a range of Reynolds number, where the maximum difference in thermal resistance is 13.8% at Re = 924. The difference at the smallest input of Reynolds number (Re = 400), which is closer to the considered condition in this study, is 0.9%. The results of this study are in good agreements with two other studies confirmed by Experimental data.
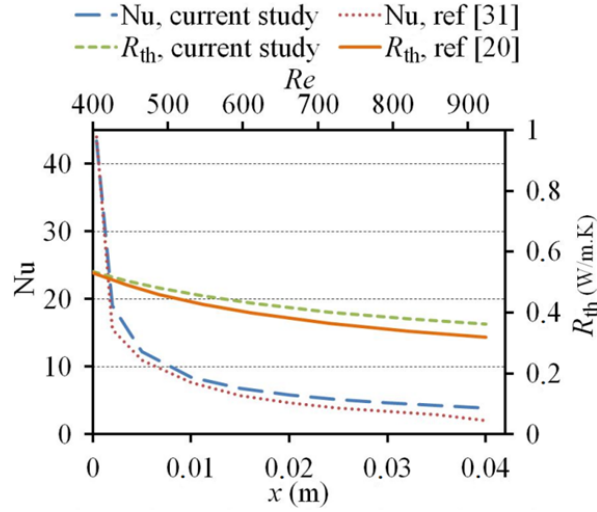
Fig. 3 Comparison of the Nusselt number in the PFHS with ref [31] ($v_i = 3$ m/s $T_i = 293.15$ K, $q = 30$ W/cm^2), and comparison of the thermal resistance of CCHS with ref [20] ($w_c = 1.5$ mm, $w_w = 1$ mm, $H_{cc} = 5$ mm).

4. Results

The aim of computational model used in this study is to demonstrate detailed results for 3D temperature distribution and voltage generation in the TEG affected by the flow in the micro-structured heat sinks. The application of the heat sinks provides realistic thermal boundary condition in the TEG in contrast to the commonly works on thermoelectricity, where the cold junction is at constant temperature. The flow temperature rises along the heat sink due to absorbing heat. Therefore, temperature on the cold junction of the thermoelements is not constant, and each thermoelement generates different voltage. However the electric potential increases in the series design of the n and p-type thermoelement, as is illustrated in Fig. 4 The effect of flow temperature variation on the temperature distribution in the thermoelements can be seen in Fig. 5 This effect is more visible at low flow velocity due to rapidly increase of the flow temperature along the heat sink. For better comparison, Table 2 shows the voltage generation in the thermoelements for sample inlet velocities.

9
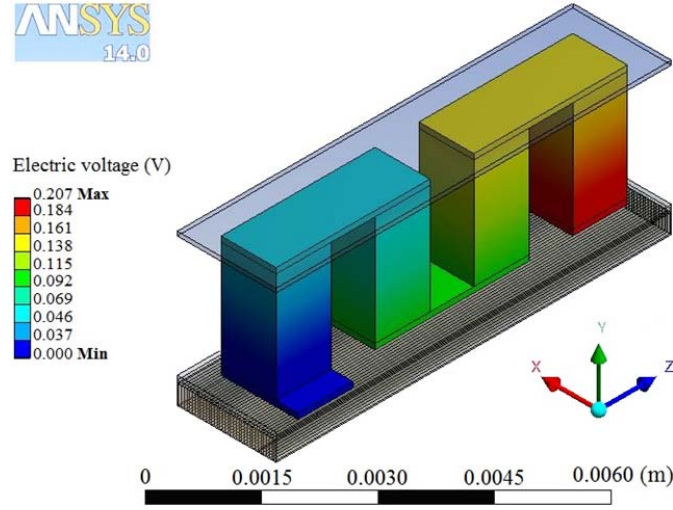
Fig. 4 Generation of the electric voltage, $v_i = 0.5$ m/s $T_h = 550$ K, $k_{teg} = 1.6$ W/m. K.
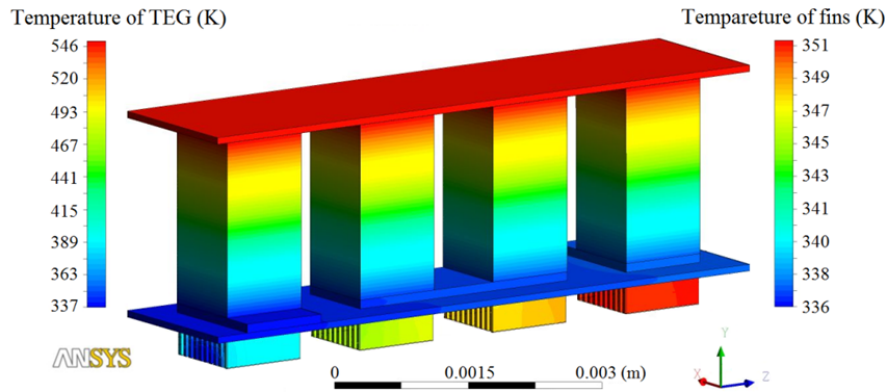
Fig. 5 Temperature distribution in the TEG and fins of CCHS, $v_i = 0.01$ m/s $T_h = 550$ K, $k_{teg} = 1.6$ W/m. K.

Table 2 Voltage generation in the thermoelements for sample inlet velocities, $T_h = 550\ K$, $k_{teg} = 1.6$ W/m. K.

v_i(m/s)	voltage generation in TEG with CCHS (V)				voltage generation in TEG with PFHS (V)			
	$TE\#1$	$TE\#2$	$TE\#3$	$TE\#4$	$TE\#1$	$TE\#2$	$TE\#3$	$TE\#4$
0.01	0,04542	0,04462	0,04428	0,04401	0,04765	0,04680	0,04634	0,04599
0.10	0,05131	0,05103	0,05085	0,05067	0,05162	0,05144	0,05132	0,05120
0.70	0,05168	0,05163	0,05160	0,05156	0,051760	0,05172	0,05171	0,05168

At higher flow rate condition, the thermal performance of the PFHS is slightly superior to the CCHS. As discussed by Kim et al. [20], for small dimensionless required pumping power, $\log\left(P_{pump}/\left(\mu^3/\left(\rho^2 D_{h,fr}\right)\right)\right)$, and large dimensionless heat sink length, $\log\left(H_c/D_{h,fr}\right)$, the PFHS is recommended. For the considered inlet velocity in this study, the dimensionless required pumping

power is smaller than 11.35 for dimensionless heat sink length equal to 1.03, where the FPHS is recommended. Moreover, at low flow rate the PFHS shows much better performance than the CCHS.

Microchannel heat sinks contain several channels in contrast to typical heat sinks with large scale channels which make it difficult to achieve constant wall temperature or constant wall heat flux. Therefore, conjugate heat transfer effect should be accounted for the microchannel heat exchangers, particularly at low Reynolds number [32]. As is mentioned in previous works [21, 33] and as Fig. 5 reveals in this study, the heat distributes in the part of the CCHS that no fin is designed. Therefore, thermal performance of the CCHS drops at the low flow inlet velocity and power generation in the TEG is less than that with PFHS. Since water is considered as the coolant fluid in this study, the temperature variation of the cold junction is limited in a small range of temperature. However suitable temperature is available on the cold junction due to relatively high specific heat capacity of the water. Therefore, as Fig. 6 shows, the voltage generation does not drop sharply when the flow inlet velocity decreases. However, the effect of the hot junction temperature dominates in voltage generation and the power generation is strongly affected by temperature difference of the cold and hot junctions (3).
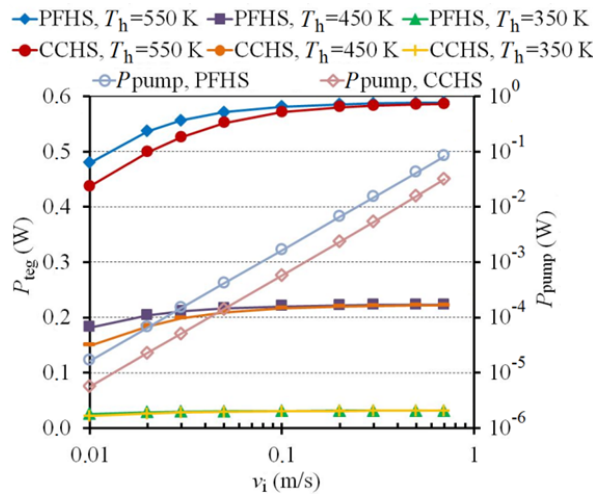
Fig. 6 Variation of electric voltage generation and required pumping power with flow inlet velocity, $k_{\text{teg}} = 1.6 \ \text{W/m.K}$.

When the system operates at high inlet velocity and low temperature difference, the net power of the system can be minus due to high required pumping power and small power generation. Therefore as Fig. 7 reveals, depending to the design of the heat sink, the limitation of inlet velocity needs to be

considered to avoid of minus net power. On the other hand, with decrease of the inlet velocity the power generation reduces, however a smaller pumping power is required due to lower pressure drop in the heat sink (8). In addition, to avoid of vaporization of the coolant fluid, there is a lower limit for the flow inlet velocity. In between of the low and high limitations of the flow inlet velocity there is an optimal point for each hot junction temperature and type of heat sink that makes maximum net power in the TEG. When the hot junction temperature increases the maximum net power occurs at higher flow inlet velocity, because the increase of the voltage generation is greater for higher hot junction temperature compared to that for small hot junction temperature.
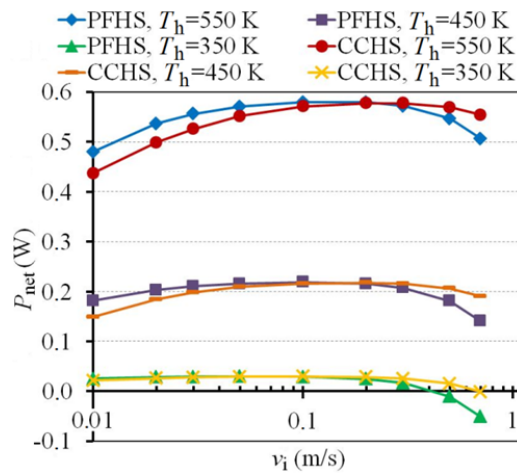
Fig. 6 Variation of thermoelectric net power with flow inlet velocity, $k_{\text{teg}} = 1.6 \ \text{W/m. K}$.

Researchers in the field of thermoelectrics have been tried to minimize thermal conductivity of the thermoelectric materials in order to provide higher temperature difference and to enhance power generation in TEGs. However, the effect of thermal conductivity needs to be considered in conjunction with the heat sink. As Fig. 8 shows, the thermal conductivity does not have strong influence on maximum value of the net power and the maximum net power is slightly superior for smaller thermal conductivity materials. However, applying smaller thermal conductivity material makes advantages of providing the maximum net power at lower inlet velocity and smaller pumping power.

Over studied range of the flow inlet velocity, the heat transfer rate in the PFHS is higher compared to the CCHS and it makes higher heat flux across the TEG (Fig. 8). For constant hot junction temperature and thermal conductivity of thermoelectric materials, the higher heat flux creates higher temperature

difference in the TEG and enhances the voltage generation. Although the required pumping power is smaller in the CCHS, the overall net power in the TEG with PFHS is slightly superior to that with CCHS. It should be noted that this evaluation is based on the particular considered microchannel dimensions, type of coolant fluid and boundary conditions.
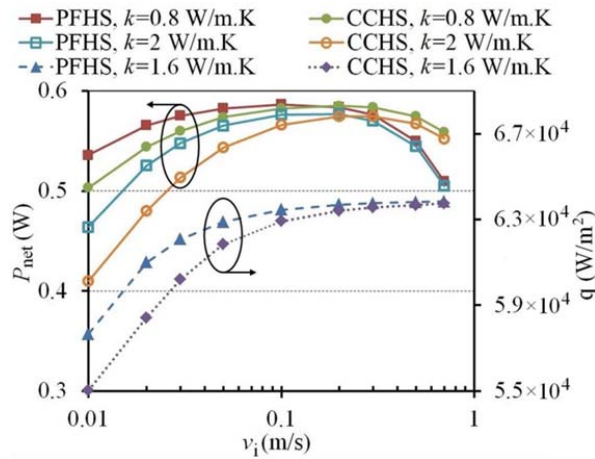
Fig. 8 Variation of thermoelectric net power and heat flux across the TEG with flow inlet velocity, $T_{\text{h}} = 550$ K.

5. Conclusions

The configuration effects of PFHS and CCHS on the power generation, the required pumping power and the net power are compared in this study over a wide range of flow inlet velocity. The 3D governing equations of thermoelectricity and flow are solved, and analysis of the model generates detailed description of the temperature distribution, voltage generation, required pumping power and the net power in the TEG through realistic thermal boundary conditions. The results illustrates that each thermoelement generates individual voltage due to effect of flow temperature variation along the heat sink. In between of the low and high limitations of the flow inlet velocity there is an optimal point for each hot junction temperature and type of heat sink that the thermoelectric net power in the module is the maximum. The results also show that, the maximum net power occurs at lower flow inlet velocity when the hot junction temperature decreases and when the thermal conductivity of the thermoelements is smaller. Thermal conductivity of thermoelectric materials does not have strong influence on maximum power generation for the considered heat sink geometries. The CCHS requires smaller pumping power but the overall net power in the TEG with PFHS is slightly superior to that with CCHS.

References

[1] P. Rosa, T.G. Karayiannis, M.W. Collins, Single-phase heat transfer in microchannels: The importance of scaling effects, Applied Thermal Engineering 29 (2009) 3447-3468.

[2] O.O. Adewumi, T. Bello-Ochende, J.P. Meyer, Constructal design of combined microchannel and micro pin fins for electronic cooling, International Journal of Heat and Mass Transfer 66 (2013) 315-323.

[3] Ercan M. Dede, Yan Liu, Experimental and numerical investigation of a multi-pass branching microchannel heat sink, Applied Thermal Engineering 55 (2013) 51-60.

[4] M. Reyes, J.R. Arias, A. Velazquez, J.M. Vega, Experimental study of heat transfer and pressure drop in micro-channel based heat sinks with tip clearance, Applied Thermal Engineering 31 (2011) 887-893.

[5] L. Chai, G. Xia, L. Wang, M. Zhou, Z. Cui, Heat transfer enhancement in microchannel heat sinks with periodic expansion–constriction cross-sections, International Journal of Heat and Mass Transfer 62 (2013) 741-751.

[6] H. Shafeie, O. Abouali, K. Jafarpur, G. Ahmadi, Numerical study of heat transfer performance of single-phase heat sinks with micro pin-fin structures, Applied Thermal Engineering 58 (2013) 68-76.

[7] A. Rezania, K. Yazawa, L.A. Rosendahl, A. Shakouri, Co-optimized design of microchannel heat exchangers and thermoelectric generators, International Journal of Thermal Sciences 72 (2013) 73-81.

[8] N. Wojtas, L. Rüthemann, W. Glatz, C. Hierold, Optimized thermal coupling of micro thermoelectric generators for improved output performance, Renewable Energy 60 (2013) 746-753.

[9] A. Rezania, L.A. Rosendahl, H. Yin, Parametric optimization of thermoelectric elements footprint for maximum power generation, Journal of Power Sources 255 (2014) 151-156.

[10] S. Zhou, B. GSammakia, B. White, P. Borgesen, Multiscale modeling of thermoelectric generators for the optimized conversion performance, International Journal of Heat and Mass Transfer 62 (2013) 435-444.

[11] J.Y. Jang, Y.C. Tsai, C.W. Wu, A study of 3-D numerical simulation and comparison with experimental results on turbulent flow of venting flue gas using thermoelectric generator modules and plate fin heat sink, Energy 53 (2013) 270-281.

[12] F.J. Lesage, É.V. Sempels, N. Lalande-Bertrand, A study on heat transfer enhancement using flow channel inserts for thermoelectric power generation, Energy Conversion and Management 75 (2013) 532-541.

[13] T.J. Hendricks, Thermal system interactions in optimizing advanced thermoelectric energy recovery systems, Journal of Energy Resources Technology 129 (2007) 223-231.

[14] X.F. Zheng, C.X. Liu, R. Boukhanouf, Y.Y. Yan, W.Z. Li, Experimental study of a domestic thermoelectric cogeneration system, Applied Thermal Engineering 62 (2014) 69-79.

[15] A. Rezania, L.A. Rosendahl, Thermal effect of ceramic substrate on heat distribution in thermoelectric generators, Journal of Electronic Materials 41 (2012) 1343-1347.

[16] A. Rezania, L.A. Rosendahl, S.J. Andreasen, Experimental investigation of thermoelectric power generation versus coolant pumping power in a microchannel heat sink, International Communications in Heat and Mass Transfer 39 (2012) 1054-1058.

[17] S.J. Kim, D.K. Kim, H.H. Oh, Comparison of fluid flow and thermal characteristics of plate-fin and pin-fin heat sinks subject to a parallel flow, Heat Transfer Engineering 29 (2008) 169-177.

[18] D. Kim, S.J. Kim, A. Ortega, Thermal optimization of microchannel heat sink with pin fin structures, Proceedings of the IMECE'03, IMECE2003-42180 (2003) 593-602.

[19] S.Y. Kim, R.L. Webb, Thermal performance analysis of fan-heat sinks for CPU cooling, Proceedings of the IMECE'03, IMECE2003-42172 (2003) 235-243.

[20] Tae Young Kim, Sung Jin Kim, Fluid flow and heat transfer characteristics of cross-cut heat sinks, International Journal of Heat and Mass Transfer 52 (2009) 5358-5370.

[21] A. Rezania, L.A. Rosendahl, New configurations of micro plate-fin heat sink to reduce coolant pumping power, Journal of Electronic Materials 41 (2012) 1298-1304.

[22] L.D. Landau, E.M. Lifshitz, Electrodynamics of continuous media, 2nd Edition, Butterworth-Heinemann, Oxford (1984).

[23] E.E. Antonova, D.C. Looman, Finite elements for thermoelectric device analysis in ANSYS, 24th International Conference on Thermoelectrics (2005) 215- 218.

[24] J.J. Shen, Z.Z. Yin, S.H. Yang, C. Yu, T.J. Zhu, X.B. Zhao, Improved thermoelectric performance of p-type bismuth antimony telluride bulk alloys prepared by hot forging, Journal of Electronic Materials, 40 (2011) 1095-1099.

[25] L.P. Hu, X.H. Liu, H.H. Xie, J.J. Shen, T.J. Zhu, X.B. Zhao, Improving thermoelectric properties of n-type bismuth–telluride-based alloys by deformation-induced lattice defects and texture enhancement, Acta Materialia 60 (2012) 4431-4437.

[26] J.P. Fleurial, L. Gailliard, R. Tribouler, H. Scherrer, S. Scherrer, Thermal properties of high quality single crystals of bismuth telluride-part i: experimental characterization, Journal of Physics and Chemistry of Solids, 49 (1988) 1237-1247.

[27] S. Ganguly, C. Zhou, D. Morelli, J. Sakamoto, C. Uher, S.L. Brock, Synthesis and evaluation of lead telluride/bismuth antimony telluride nanocomposites for thermoelectric applications, Journal of Solid State Chemistry 184 (2011) 3195-3201.

[28] R.A. Serway, Principles of Physics, 2nd ed., Fort Worth, Texas; London: Saunders College Publishing (1998) 602.

[29] M.I. Hasan, Investigation of flow and heat transfer characteristics in micro pin fin heat sink with nanofluid, Applied Thermal Engineering 63 (2014) 598-607.

[30] M. Chen, L.A. Rosendahl, T. Condra, A three-dimensional numerical model of thermoelectric generators in fluid power systems, International Journal of Heat and Mass Transfer 54 (2011) 345-355.

[31] Y. Chen, C. Zhang, M. Shi, J. Wu, Three-dimensional numerical simulation of heat and fluid flow in noncircular microchannel heat sinks, International Communications in Heat and Mass Transfer 36 (2009) 917-920.

[32] G.L. Morini, Scaling effects for liquid flows in microchannels, Heat Transfer Engineering 27 (2006) 64‑73.

[33] Shan Yin, King Jet Tseng, Jiyun Zhao, Design of AlN-based micro-channel heat sink in direct bond copper for power electronics packaging, Applied Thermal Engineering 52 (2013) 120-129.

Appendix B

```
%    Nonlinear equation system for PVTEG


%    Temperature index
%    Tpvg=T1
%    Tpvtop=T2
%    Tpv=T3
%    Tcrh=T4
%    Ttegh=T5
%    Ttegc=T6
%    Tcrc=T7

%    Equations:

%    #1-A
%    (Ac*Hwh+Ac*kpvg/L1)T1-(Ac*kpvg/L1)T2=Ac*Hwh*Ta

%    #2-B
%    -(Ac*kpvg/L1)T1+(Ac*kpvg/L1+Ac*(kEva/L21+kSi/L22))T2-(Ac*↙
(kEva/L21+kSi/L22)+Gt*Eref*Bref)T3=Gt-E*S*Ac*(T2^4-Tsky^4)

%    #3-C
%    -(Ac*(kEva/L21+kSi/L22))T2+(Ac*(kEva/L21+kSi/L22)+Ac*↙
(kSi/L31+kEva/L32)+0.5*Gt*Eref*Bref)T3-(Ac*(kSi/L31+kEva/L32))T4=-↙
Gt*Eref*(1+Bref*Tref)

%    #4-D
%    -(Ac*(kSi/L31+kEva/L32))T3+(Ac*(kSi/L31+kEva/L32)+Ac*kcrh/L4)T4-↙
(Ac*kcrh/L4)T5=0

%    #5-E
%    -(Ac*kcrh/L4)T4+(Ac*kcrh/L4+Ateg*kteg/L5)T5-(Ac*kteg/L5)T6=-Pteg=↙
-0.5*((T5-T6)/T5)*((sqrt(1+ZT)-1)/(sqrt(1+ZT)+T6/T5))*(Gt-Gt*Eref*(1-↙
Bref*(T3-Tref))-E*S*Ac*(T2^4-Tsky^4))

%    #6-F
%    -(Ateg*kteg/L5)T5+(Ateg*kteg/L5+Ac*kcrc/L6)T6-(Ac*kcrc/L6)T7=Pteg=-↙
0.5*((T5-T6)/T5)*((sqrt(1+ZT)-1)/(sqrt(1+ZT)+T6/T5))*(Gt-Gt*Eref*(1-↙
Bref*(T3-Tref))-E*S*Ac*(T2^4-Tsky^4))

%    #7-G
%    -(Ac*kcrc/L6)T6+(Ac*kcrc/L6+Ac*Hwc)T7=Ac*Hwc*Ta
```

```matlab
%    hw:=5.678*(a+b*((294.26/(273.16+Ta))*Vm/.3048)^n)
%    if Vm<4.88 m/s, a=0.99, b=0.21, n=1
%    if 4.88<Vm<30.48 m/s, a=0, b=0.5, n=0.78




function solveeqs()
guess=[310 309 308 307 306 305 304];
[result, fval, exit, output]=fsolve(@eqnb,guess);
result;

Tglass=result(1,1)
TpvTop=result(1,2)
Tpv=result(1,3)
Tcrh=result(1,4)
Ttegh=result(1,5)
Ttegc=result(1,6)
Tcrc=result(1,7)



fval;
eqnb(guess);
output;
end

function fcns=eqnb(z)

Ac=1;
%Variable Parameters
Gt=10000*0.9*Ac;
Ta=285;
ZT=1;
Vm=5;
f=0.4;

% reference 12 (Lu & Yao) of Ref 73
kpvg=0.9;
L1=0.003;

kEva=0.35;
L21=0.0005;
kSi=148;
```

```matlab
L22=0.0002;
L31=0.0002;
L32=0.0005;


%PV efficiency: Ref 66
Eref=0.12;
Bref=0.0045;
Tref=298;

%TEG
kcrh=30;
L4=0.0005;
Ateg=f*Ac;
kteg=1.2;
L5=0.0002;
kcrc=30;
L6=0.0005;

%   radiation Heat transfer coefficient-Ref 69
Ef=0.9;      %Emissivity Coefficient
Er=0.85;     %Rear surface Emissivity Coefficient- reference 32 of Ref↙
73
S=5.67*10^(-8);     %Stefan-Boltzmann constant
Tsky=0.0553*(Ta)^1.5;    %Sky temperature-Ref 70



% Natural Convection Constants
Grcr=10^9;
theta=0.6105;
v=1.51267^(-05);
kair= 0.0257;
Pr= 0.713;
beta=0.00343;
g= 9.81;
L= Ac^(1/2);




%   Heat transfer coefficient-Ref 69
%   Front surface of PV
Tac=Ta-273.15;
if (Vm<4.88)Hwh=5.678*(0.99+0.21*((294.26/(273.16+Tac))*Vm/.3048)^1);
else Hwh=5.678*(0.5*((294.26/(273.16+Tac))*Vm/.3048)^0.78);
```

```matlab
end
%Hwh=0;

%   Back surface of PV
if (Vm<4.88)Hwc=5.678*(0.99+0.21*((294.26/(273.16+Tac))*Vm/.3048)^1);
else Hwc=5.678*(0.5*((294.26/(273.16+Tac))*Vm/.3048)^0.78);
end
%Hwc=100000;



%   #1-A
A1=(Ac*Hwh+Ac*kpvg/L1);
A2=-(Ac*kpvg/L1);
A3=0;
A4=0;
A5=0;
A6=0;
A7=0;

%   #2-B
B1=-(Ac*kpvg/L1);
B2=(Ac*kpvg/L1+Ac*(kEva/L21+kSi/L22));
B3=-(Ac*(kEva/L21+kSi/L22));
B4=0;
B5=0;
B6=0;
B7=0;
B=0;

%   #3-C
C1=0;
C2=-(Ac*(kEva/L21+kSi/L22));
C3=(Ac*(kEva/L21+kSi/L22)+Ac*(kSi/L31+kEva/L32)-Gt*Eref*Bref);
C4=-(Ac*(kSi/L31+kEva/L32));
C5=0;
C6=0;
C7=0;
C=-Gt*Eref*(1+Bref*Tref);

%   #4-D
D1=0;
D2=0;
D3=-(Ac*(kSi/L31+kEva/L32));
D4=(Ac*(kSi/L31+kEva/L32)+Ac*kcrh/L4);
```

```matlab
D5=-(Ac*kcrh/L4);
D6=0;
D7=0;
D=0;

%    #5-E
E1=0;
E2=0;
E3=0;
E4=-(Ac*kcrh/L4);
E5=(Ac*kcrh/L4+Ateg*kteg/L5);
E6=-(Ateg*kteg/L5);
E7=0;

%    #6-F
F1=0;
F2=0;
F3=0;
F4=0;
F5=-(Ateg*kteg/L5);
F6=(Ateg*kteg/L5+Ac*kcrc/L6);
F7=-(Ac*kcrc/L6);

%    #7-G
G1=0;
G2=0;
G3=3;
G4=0;
G5=0;
G6=-(Ac*kcrc/L6);
G7=(Ac*kcrc/L6+Ac*Hwc);
G=Ac*Hwc*Ta;


T1=z(1);
T2=z(2);
T3=z(3);
T4=z(4);
T5=z(5);
T6=z(6);
T7=z(7);

fcns(1)=A1*T1+A2*T2-Ac*Hwh*Ta+Ac*((0.14*(g*cos(theta)*beta*(T1-Ta) ↵
*L^3*Pr/v^2)^(1/3)-0.14*(Grcr*Pr)^(1/3)+0.56*(Grcr*Pr*cos(theta))^ ↵
```

```
(1/4))*kair/L)*(T1-Ta);
fcns(2)=B1*T1+B2*T2+B3*T3-Gt+Ef*S*Ac*(T2^4-Tsky^4);
fcns(3)=C2*T2+C3*T3+C4*T4-C;
fcns(4)=D3*T3+D4*T4+D5*T5-D;
fcns(5)=E4*T4+E5*T5+E6*T6+0.5*((T5-T6)/T5)*((sqrt(1+ZT)-1)/(sqrt(1+ZT) ↙
+T6/T5))*(Gt-Gt*Eref*(1-Bref*(T3-Tref))-Ef*S*Ac*(T2^4-Tsky^4));
fcns(6)=F5*T5+F6*T6+F7*T7+0.5*((T5-T6)/T5)*((sqrt(1+ZT)-1)/(sqrt(1+ZT) ↙
+T6/T5))*(Gt-Gt*Eref*(1-Bref*(T3-Tref))-Ef*S*Ac*(T2^4-Tsky^4));
fcns(7)=G6*T6+G7*T7-G;
end
```

Appendix C1

Appendix P, regularly updated:

Ver 2012.1

Project Number: 12045

Title: Integrated Photovoltaics with Thermoelectrics

	Original end-date	1-Dec-2013	Duration	12 Month
	Finalized	1-Dec-2013	Duration	12 Month
	Extension / Delay			0 Month

Budget (DDKx1000)

Budget	Total	PSO funding	Other funding	Internal
Contract sum	554,7	500,0	-	54,6
Supplementary grant 1				
Supplementary grant 2				
Total	**554,7**	**500,0**	**-**	**54,6**

	Start	End
Previous periods:	01-04-2013	31-12-2013

	Total	PSO funding	Other funding	Internal
Accumulated costs (periods in this worksheet)	573,8	517,9	-	55,9
Residual sum / residual commitment	(19,1)	(17,9)	-	(1,3)

Net expenses realised during the periods (sum of periods)

	Start date	End date	Total	PSO funding	Other funding	Internal
Phase 1	01-01-13	30-06-13	382,5	343,1	-	39,4
Phase 2	01-07-13	31-12-13	191,3	174,8	-	16,5
Phase 3			-	-	-	-
Phase 4			-	-	-	-
Phase 5			-	-	-	-
Phase 6			-	-	-	-
Phase 7			-	-	-	-
Phase 8			-	-	-	-
Phase 9			-	-	-	-
Phase 10			-	-	-	-
Phase 11			-	-	-	-
Phase 12			-	-	-	-
Phase 13			-	-	-	-
Phase 14			-	-	-	-
Phase 15			-	-	-	-
Accumulated costs			**573,8**	**517,9**	**1**	**55,9**

Budget, reporting and payment plan

PSO sum exceeded! Contact Energinet.dk to reduce PSO share of expences.

Budget	Project month	End period	Reporting	PSO share krx1000
	7 th. month	30-06-13	juli 2013	250
	13 th. month	31-12-13	januar 2014	250
	13 th. month	00-01-00	januar 1900	0
	13 th. month	00-01-00	januar 1900	0
	13 th. month	00-01-00	januar 1900	0
	13 th. month	00-01-00	januar 1900	0
	13 th. month	00-01-00	januar 1900	0
	13 th. month	00-01-00	januar 1900	0
	13 th. month	00-01-00	januar 1900	0
	13 th. month	00-01-00	januar 1900	0
	13 th. month	00-01-00	januar 1900	0
	13 th. month	00-01-00	januar 1900	0
	13 th. month	00-01-00	januar 1900	0
	13 th. month	00-01-00	januar 1900	0
				500,0

Account/budget keyfigures

Partner		Total	PSO funding	Other funding	Internal
29102384 Energiteknik, Aalborg Universitet					
31119103 Aarhus University					
32787185 Alpcon A/S					
28860323 Dansk Solenergi ApS					
Accumulated costs		**573,8**	**517,9**	**-**	**55,9**

Budget		Total	Internal	Other funding	PSO
		554,7	54,6	-	500,1
		584,7	54,6	-	500,1

Signature (when finalized)